Journal of Harbin Institute of Technology (*New Series*)

Citation: Shuangmin Li , Congpeng Shao, Haojie Xu, et al. Influences of nominal radial clearance on lubrication and dynamic performances of bump air foil bearing. *Journal of Harbin Institute of Technology* (*New Series*). DOI: 10.11916/j.issn.1005-9113.24049

Influences of Nominal Radial Clearance on Lubrication and Dynamic Performances of Bump Air Foil Bearing

Shuangmin Li[1], *Congpeng Shao*[1], *Haojie Xu*[2] *and Qi An*[1 *]

(*1. School of Mechanical and Power Engineering*, *East China University of Science and Technology*, *Shanghai 200237*, *China*;
2. Yangtze Delta Region Institute of Tsinghua University, *Jiaxing 314000*, *Zhejiang*, *China*)

Abstract: In the design of air foil bearings, nominal radial clearance is an important parameter that affects bearing performance. To analyze radial clearance influence on bearing lubrication and dynamic performance, a mechanical model that simplifies the foil structure as a two-dimensional thin plate finite element model with an elastic support is established using the theory of elasticity. The calculation model comprehensively considers the interactive forces of bumps and the frictions between the top foil and bump foil, as well as between the bump foil and bearing bushing. A flow-solid coupling calculation model is established based on the compressible gas Reynolds equation. By using perturbation methods, the calculation model for bearing dynamic performance is established. The reliability of the model is verified through experiments measuring the friction torque of the bearing. Through a specific case study, the influences of radial clearance and rotational speed on lubrication and dynamic performance are calculated. In addition, the influence of the foil's structural parameters on bearing performances is also studied.

Keywords: air foil bearing; radial clearance; fluid-solid coupling; lubrication performances; dynamic performances

CLC number: TH133.35; TH117.2 **Document code**: A **Article ID**: 1005-9113(2026)00-0000-23

0 Introduction

Currently, air foil bearings are critical for extreme-condition rotating systems[1-2]. Among various air foil bearings, bump-type air foil bearings are the most successful and widely implemented design[3]. The radial clearance of bump air foil journal bearings is one of the crucial parameters affecting their lubrication and dynamic performance, but relevant studies are not yet sufficient. Consequently, it is necessary to comprehensively study the influence of radial clearance on the performance of the bump air foil journal bearing.

Walowit et al.[4] conducted theoretical analysis on bump foil journal bearings, and established an elastic deformation model of foil structure for the first time to determine its elastic coefficients. Heshmat et al.[5-6] simplified the bump foil as a linear spring and developed an analytical solution for gas film thickness considering foil deformation. The bearing capacity of the foil bearings was assessed. Radil et al.[7] examined the influence of radial clearance on bearing load capacity. The bearing had an optimal radial clearance introducing a maximum load capacity coefficient when frictional heat was considered. To obtain an optimal foil structure, many studies about the influence of structural parameters on bearing performance have been conducted, including length-to-diameter ratio, foil flexibility and thickness, and the size parameters of the bump arch. These studies investigated how these parameters affect the vibration of the supported rotor and the performance of the bearing[8-12]. Mahner et al.[13-15] proposed a fully coupled thermoelastic gas dynamic pressure model. The effects of mechanical preload on the thermodynamics, startup friction torque, and other performances of three-lobed foil gas bearings were investigated through computational and experimental analyses. Kim[16] conducted a comparative analysis of load capacity, stiffness

---

Received 2024-08-14.

Sponsored by Shanghai Design Ⅳ Peak Discipline "Modern Mechanical Theory Research and Related Product Development" Special Fund (Grant No. DA17014).

[*] Corresponding author: Qi An, Ph.D., Professor. Email: anqi@ecust.edu.cn

distribution, and bearing stability with single and three-lobed foil structures. It showed that foil bearings with a single lobe have a greater load capacity but have lower onset speeds of instability. Shi et al.[17-19] analyzed how rotational speed, nominal clearance, bump foil geometry, and loading direction affect the two types of bearings. It was discovered that the load capacity of bearings was significantly influenced by nominal clearance, and load capacity decreases with increasing nominal clearance. Guan and Feng[20] coupled an elastic mechanical model with compressible gas Reynolds equation to predict bearings' static and dynamic performances, and found that the dynamic main stiffness and damping coefficients increase with decreasing nominal clearance. Sim et al.[21] and Walter et al.[22] found that the minimum clearances affect the dynamic performances and stability of bearings. Xiong et al.[23] analyzed effects of different foils' friction coefficients on the dynamic performance based on CFD methods, and revealed that dynamic stiffness and damping coefficients are underestimated when friction coefficient exceeds 0.3. Cheng et al.[24] proposed a method for identifying dynamic coefficients of bearings. The frequency response function and equivalent coefficient methods were used to identify the dynamic coefficients.

Load capacity, stability, and vibration damping of air foil bearings depend critically on the bump foil[25]. Arghir and Benchekroun [26] proposed a contact mechanics model based on a structural model of bump foil bearings, which considered gaps and close/loose contacts in the foils and was more accurate in simulating manufacturing errors in the foils. A novel fully-coupled elastic-fluid model capturing foil contact/separation/friction dynamics was developed by Gu et al.[27]. By employing a double-layered foil, adjusting the layout of the foils and increasing the thickness of the foils, Xu et al.[28-29] increased the bearing's structural stiffness and experimentally verified that double-layered foils could enhance the bearing damping. By adding four layers of foil to the bearing, Li et al.[30] examined the mechanical relationship of contact between each layer of foil. Zhao et al.[25] analyzed the Coulomb damping dissipation performance based on a two-dimensional mechanical model. Liang et al.[31] used 3D FEM to analyze the influences of structural parameters of bump foil on bearing load capacity. The results showed that the bump arch width was an important parameter affecting the load capacity of bearings, while the bump arch height minimally affected the bump foil stiffness.

It can be seen that radial clearance is a crucial geometric parameter that affects the performances of air foil bearings. However, its influence on bearing dynamic performance was rarely investigated according to the literature analysis. Therefore, a mechanical model simplifying the foil structure of the bearing as a two-dimensional thin plate finite element model with an elastic support was established using the theory of elasticity in Section 1. Friction behaviors between bump foil-top foil and bump foil-bearing bushing interfaces were incorporated. Then, the mechanical model of bearing is coupled with the compressible gas Reynolds equation. Subsequently, the reliability of the proposed model is verified by experiments in Section 2.1. This study numerically investigates how radial clearance and foil structural parameters affect bearing lubrication and dynamic performance.

1 Mechanical Modelling

1.1 Establishment of Lubrication Mechanical Model

Fig. 1 shows the position relationship between the bump air foil bearing and rotor before and during operation, where O_b and O_r are the bearing's center and rotor's center, respectively. When the bearing is operating, elastic deformation of bumps is caused by the air film pressure shown in Fig. 2(a). Contrary to Ref.[11], the mechanical model of bump foil bearing developed more comprehensively considers friction forces, stiffness of foils, damping of foils and interactive forces between bumps, which can more realistically reflect the performance of the bearing. The force analysis of the foils is carried out under the following assumptions:

1) The bumps are always in contact with the inner surface of the bearing bushing.

2) The bumps' displacements in the circumferential direction are from the fixed end to the free end.

3) The force is focused on the top of the bumps.

4) The deformation of the bump and top foils is within the elastic range during operation.

The force diagram of bumps is shown in Figs. 2(b)-(d). f represents friction. F_{left} and F_{right}

represent the interactive forces between bumps. Vertical loads F, F_1 and F_2 act on the top, left, and right sides of each bump, respectively. The bump foil deformation w_b is calculated using Castigliano's second theorem. As shown in Fig. 2(b), the forces balance equation in horizontal and vertical directions and the moment balance equations of a bump can be obtained as follows:

$$\begin{cases} F_{\text{left}} - F_{\text{right}} - f - f_1 - f_2 = 0 \\ F - F_1 - F_2 = 0 \\ Fl + f(R_0 - R_0\cos\varphi) - F_1(2l) = 0 \end{cases} \tag{1}$$

where $f = \eta F$, $f_1 = \eta_1 F_1$, $f_2 = \eta_1 F_2$, η and η_1 are friction coefficients between bump foil-top foil and bump foil-bearing bushing, R_0 is bump arch radius, l is bump arch half-length, φ is bump arch half-angle. F_a is the horizontal right additional force.

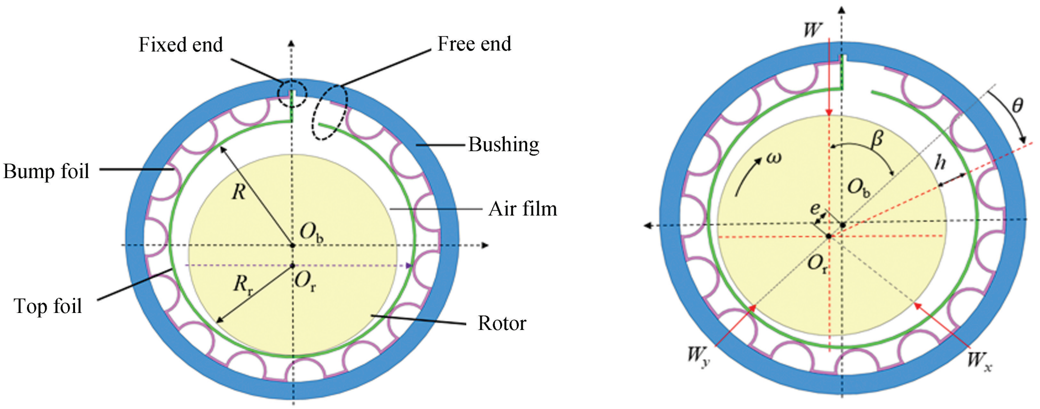

(a) Before operation

(b) During operation

Fig.1 Schematic diagram of the foil bearing

The bending moment of a bump is:

$$\begin{cases} M_v = \left[(\eta + \eta_1)F + F_{\text{right}} - \eta_1 \dfrac{l + \eta R_0(1 - \cos\varphi)}{2l} F \right] R_0 [\cos(\varphi - \alpha) - \cos\varphi] - \\ \quad \dfrac{l + \eta R_0(1 - \cos\varphi)}{2l} [l - R_0 \sin(\varphi - \alpha)] F, 0 \leqslant \alpha \leqslant \varphi \\ M_{h1} = \left[(\eta + \eta_1)F + F_{\text{right}} - F_a - \dfrac{Fl + (\eta F - F_a) R_0 (1 - \cos\varphi)}{2l} \right] R_0 [\cos(\varphi - \alpha) - \cos\varphi] - \\ \quad \dfrac{Fl + (\eta F - F_a) R_0 (1 - \cos\varphi)}{2l} [l - R_0 \sin(\varphi - \alpha)], 0 \leqslant \alpha \leqslant \varphi \\ M_{h2} = \left[\eta_1 \dfrac{l - \eta R_0 (1 - \cos\varphi)}{2l} F + F_{\text{right}} - F_a \right] R_0 [\cos(\alpha - \varphi) - \cos\varphi] - \\ \quad \dfrac{l - \eta R_0(1 - \cos\varphi)}{2l} [l - R_0 \sin(\alpha - \varphi)] F, \varphi \leqslant \alpha \leqslant 2\varphi \end{cases} \tag{2}$$

Applying Castigliano's second theorem and integrating over Eq. (2), the vertical and horizontal deformations of the bump can be obtained as follows:

$$\begin{cases} w_b = \displaystyle\int_0^{\varphi} \frac{M_v}{EI} \frac{\partial M_v}{\partial F} R_0 \mathrm{d}\alpha \\ \Delta x_1 = \left[\displaystyle\int_0^{\varphi} \frac{M_{h1}}{EI} \frac{\partial M_{h1}}{\partial F_a} R_0 \mathrm{d}\alpha \right]_{F_a = 0} \\ \Delta x_2 = \left[\displaystyle\int_0^{\varphi} \frac{M_{h2}}{EI} \frac{\partial M_{h2}}{\partial F_a} R_0 \mathrm{d}\alpha \right]_{F_a = 0} \end{cases} \tag{3}$$

The bump is equated to a spring with damping as shown in Fig. 2 (a), and the bump arch stiffness is as follows:

$$K_b = \frac{\partial F}{\partial w_b} \tag{4}$$

The damping C_b of a bump can be expressed as follows[32-33]:

$$C_b = \zeta \frac{K_b}{\omega_e} \tag{5}$$

where ζ is proportional damping coefficient, ω_e is vortex frequency. $F = 0$ at the non-contact position of the bump and top foils. The total stiffness and damping matrices K_b, C_b of the bump foil are obtained by integrating K_b and C_b.

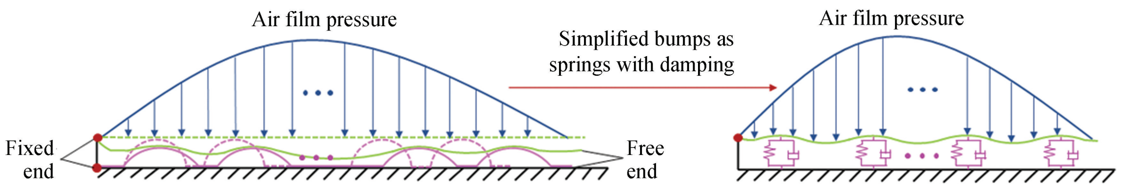

(a) Deformation of foils and equivalence model of the bump

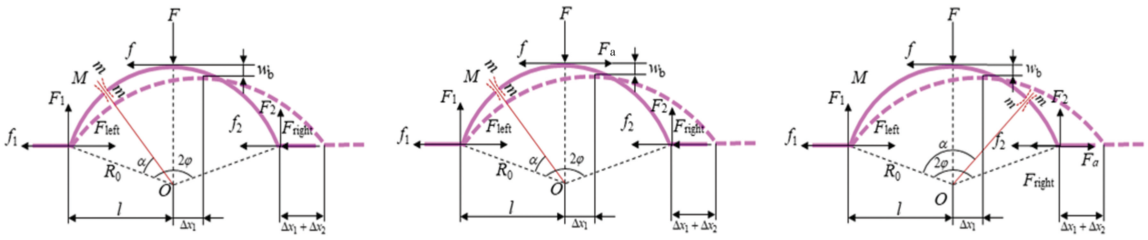

(b) Vertical deformation (c) Left horizontal deformation (d) Right horizontal deformation

Fig. 2 Schematic of the force and deformation of the bump foil

The thin plate theory is used to establish the finite element model of the top foil (as shown in Fig. 3). The top foil deformation is smaller than the thickness t_t, so the small deflection theory is adopted to improve calculation accuracy.

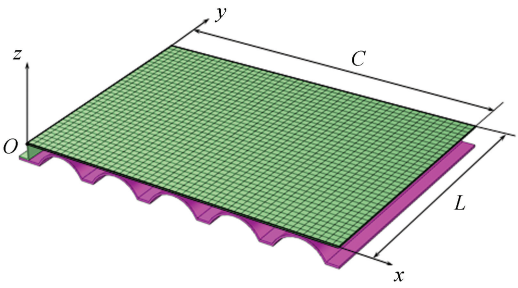

Fig.3 Schematic of the finite element model of the top foil

As shown in Fig.4(a), the top foil is discretized using rectangular elements. The element dimensions are a, b in x and y directions, respectively. A rectangular element includes four nodes (i, j, m, n). The displacements and forces of the node are expressed as shown in Eq.(6):

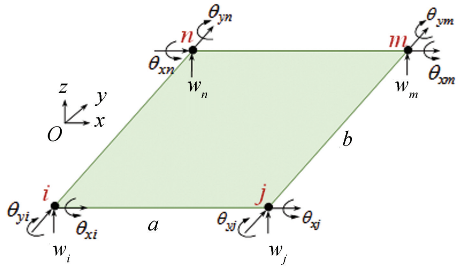

(a) Diagram of rectangular element

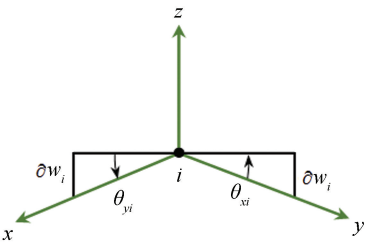

(b) Diagram of node displacements

Fig. 4 Schematic diagram of a rectangular thin plate element

$$\begin{cases} \boldsymbol{q}_e = [w_i \quad \theta_{xi} \quad \theta_{yi} \quad w_j \quad \theta_{xj} \quad \theta_{yj} \quad w_m \quad \theta_{xm} \quad \theta_{ym} \quad w_n \quad \theta_{xn} \quad \theta_{yn}]^{\mathrm{T}} \\ \boldsymbol{F}_e = [F_{zi} \quad M_{xi} \quad M_{yi} \quad F_{zj} \quad M_{xj} \quad M_{yj} \quad F_{zm} \quad M_{xm} \quad M_{ym} \quad F_{zn} \quad M_{xn} \quad M_{yn}]^{\mathrm{T}} \end{cases} \tag{6}$$

The displacement function during the bending of a thin plate can be expressed as follows:

$$w_t(x,y) = \kappa_1 + \kappa_2 x + \kappa_3 y + \kappa_4 x^2 + \kappa_5 xy + \kappa_6 y^2 + \kappa_7 x^3 + \kappa_8 x^2 y + \kappa_9 xy^2 + \kappa_{10} y^3 + \kappa_{11} x^3 y + \kappa_{12} xy^3 \tag{7}$$

Taking node i as an example, according to the geometric relationship (as shown in Fig. 4(b)), the approximation is taken as $\sin\theta_{xi} = \theta_{xi}$, and $\sin\theta_{yi} = \theta_{yi}$. Then $\theta_{xi} = \partial w_i / \partial y_i$, $\theta_{yi} = -\partial w_i / \partial x_i$. Similarly, nodes j, m, n are processed as above and the 12 coefficients $\kappa_1, \kappa_2, \ldots, \kappa_{11}, \kappa_{12}$ of Eq. (7) are obtained. The deflection matrix of rectangular elements is:

$$w_t(x,y) = \boldsymbol{N}\boldsymbol{q}_e \tag{8}$$

where N is the shape function of rectangular elements and expressed as:

$$\boldsymbol{N} = [\boldsymbol{N}_i\ \boldsymbol{N}_j\ \boldsymbol{N}_m\ \boldsymbol{N}_n] = [N_i \quad N_{xi} \quad N_{yi} \quad N_j \quad N_{xj} \quad N_{yj} \quad N_m \quad N_{xm} \quad N_{ym} \quad N_n \quad N_{xn} \quad N_{yn}] \tag{9}$$

where N_i , N_{xi} , N_{yi} ,⋯, N_n , N_{xn} , N_{yn} are expressed as follows:

$$\begin{cases} N_g = \dfrac{1}{8}\left(1 + \dfrac{x}{x_g}\right)\left(1 + \dfrac{y}{y_g}\right)\left[2 + \dfrac{x}{x_g}\left(1 - \dfrac{x}{x_g}\right) + \right. \\ \qquad \left. \dfrac{y}{y_g}\left(1 - \dfrac{y}{y_g}\right)\right] \\ N_{xg} = -\dfrac{1}{8}y_g\left(1 + \dfrac{x}{x_g}\right)\left(1 + \dfrac{y}{y_g}\right)^2\left(1 - \dfrac{y}{y_g}\right) \\ N_{yg} = -\dfrac{1}{8}x_g\left(1 + \dfrac{x}{x_g}\right)\left(1 + \dfrac{y}{y_g}\right)^2\left(1 - \dfrac{x}{x_g}\right) \end{cases} \tag{10}$$

where $g = i, j, m, n$.

The stress matrix of a rectangular element is:

$$\boldsymbol{B}_e = [\boldsymbol{B}_i\ \boldsymbol{B}_j\ \boldsymbol{B}_m\ \boldsymbol{B}_n] = -\begin{bmatrix} \dfrac{\partial^2}{\partial x^2} \\ \dfrac{\partial^2}{\partial y^2} \\ 2\dfrac{\partial^2}{\partial x \partial y} \end{bmatrix}^{\mathrm{T}} \cdot \boldsymbol{N} \tag{11}$$

The stiffness matrix for rectangular elements is:

$$K_{\mathrm{te}} = \frac{t_{\mathrm{t}}^3}{12}\iint_A \boldsymbol{B}_{\mathrm{e}}^{\mathrm{T}} \boldsymbol{D}_{\mathrm{e}} \boldsymbol{B}_{\mathrm{e}} \mathrm{d}x\mathrm{d}y \tag{12}$$

The damping matrix for rectangular elements[32] is:

$$\boldsymbol{C}_{\mathrm{te}} = \zeta \frac{\boldsymbol{K}_{\mathrm{te}}}{\boldsymbol{\omega}_{\mathrm{e}}} \tag{13}$$

where $\boldsymbol{D}_{\mathrm{e}}$ is the elastic matrix and is expressed as follows:

$$\boldsymbol{D}_{\mathrm{e}} = \frac{E}{1 - u_{\mathrm{b}}}\begin{bmatrix} 1 & u_{\mathrm{b}} & 0 \\ u_{\mathrm{b}} & 1 & 0 \\ 0 & 0 & \dfrac{1 - u_{\mathrm{b}}}{2} \end{bmatrix} \tag{14}$$

where E is the elasticity modulus of foils, u_{b} is Poisson's ratio of foils. The top foil overall stiffness $\boldsymbol{K}_t$ is obtained by standard integration rules. The force matrix on the top foil is recorded as $\boldsymbol{F}$. The relationship of $\boldsymbol{K}_{\mathrm{t}}$ and $\boldsymbol{F}$ is:

$$\boldsymbol{F} = \boldsymbol{K}_{\mathrm{t}}\boldsymbol{q} \tag{15}$$

where $\boldsymbol{q}$ is the top foil overall displacement matrix. Total bearing stiffness and damping result from combined top and bump foil contributions, i.e. $\boldsymbol{K}_{\mathrm{f}} = \boldsymbol{K}_{\mathrm{t}} + \boldsymbol{K}_{\mathrm{b}}$ and $\boldsymbol{C}_{\mathrm{f}} = \boldsymbol{C}_{\mathrm{t}} + \boldsymbol{C}_{\mathrm{b}}$.

Thus, the lubricating air film thickness is:

$$h = c + e\cos\theta + w_{\mathrm{t}} \tag{16}$$

where $c = R - R_{\mathrm{r}}$ is nominal radial clearance. R is bearing radius. R_{r} is rotor radius. e is eccentricity distance. The dimensionless form of Eq. (16) is:

$$H = \frac{h}{c} = 1 + \varepsilon\cos\theta + \bar{w}_{\mathrm{t}} \tag{17}$$

where ε is eccentricity of the bearing.

The formula for the ideal gas state is:

$$\frac{p}{\rho} = \Re T \tag{18}$$

Neglecting pressure-dependent viscosity, the isothermal compressible Reynolds equation simplifies to:

$$\frac{\partial}{\partial x}\left(ph^3 \frac{\partial p}{\partial x}\right) + \frac{\partial}{\partial z}\left(ph^3 \frac{\partial p}{\partial z}\right) = 6\mu U \frac{\partial}{\partial x}(ph) + 12\mu \frac{\partial}{\partial t}(ph) \tag{19}$$

Eq. (19) is dimensionless:

$$\frac{\partial}{\partial\theta}\left(PH^3 \frac{\partial P}{\partial\theta}\right) + \frac{4R^2}{L^2}\frac{\partial}{\partial\lambda}\left(PH^3 \frac{\partial P}{\partial\lambda}\right) = \Lambda \frac{\partial}{\partial\theta}(PH) + 2\Lambda v \frac{\partial}{\partial\tau_e}(PH) \tag{20}$$

where $x = R\theta$, $H = \dfrac{h}{c}$, $z = \lambda \dfrac{L}{2}$, $P = \dfrac{p}{p_0}$, $\Lambda = \dfrac{6\mu UR}{c^2 p_0}$, $U = \omega R_{\mathrm{r}}$, $v = \dfrac{\omega_{\mathrm{e}}}{\omega}$, $\tau_{\mathrm{e}} = \omega_{\mathrm{e}} t$. λ is dimensionless length in axial width direction, Λ is bearing number, τ_{e} is dimensionless time, ω is rotor angular velocity.

1.2 Calculation Model for Lubrication Performances

The static air film pressure of bearings is determined by the static operating point and is independent of time[34]. When the bearing is in a stable operation, the lubricating air exhibits steady flow. Thus, the compressible gas Reynolds equation is as follows:

$$\frac{\partial}{\partial\theta}\left(PH^3 \frac{\partial P}{\partial\theta}\right) + \frac{4R^2}{L^2}\frac{\partial}{\partial\lambda}\left(PH^3 \frac{\partial P}{\partial\lambda}\right) = \Lambda \frac{\partial}{\partial\theta}(PH) \tag{21}$$

The boundary conditions of dimensionless pressure during the solution of lubrication performances are:

$$\begin{cases} P(0,\lambda) = 1 \\ P(\theta_{\mathrm{free}},\lambda) = 1 \\ P(\theta,\lambda = \pm 1) = 1 \end{cases} \tag{22}$$

As shown in Fig.1, the bearing load capacity W consists of W_x and W_y during the stable operation, which can be calculated as follows:

$$W_x = \int_{-1}^{1} \int_{0}^{\theta_{\mathrm{free}}} (P - 1)\sin\theta \mathrm{d}\theta \mathrm{d}\lambda \tag{23a}$$

$$W_y = -\int_{-1}^{1} \int_{0}^{\theta_{\mathrm{free}}} (P - 1)\cos\theta \mathrm{d}\theta \mathrm{d}\lambda \tag{23b}$$

$$W = \sqrt{W_x{}^2 + W_y{}^2} \tag{24}$$

The viscous friction torque of the lubricating film acting on the surface of the shaft is expressed as follows:

$$T_{\mathrm{r}} = \frac{cp_0LR}{4} \int_{-1}^{1} \int_{0}^{\theta_{\mathrm{free}}} \left(H \frac{\partial P}{\partial \theta} + \frac{\Lambda}{3} \frac{1}{H}\right) \mathrm{d}\theta \mathrm{d}\lambda \tag{25}$$

The friction power loss to overcome the viscous friction torque is expressed as follows:

$$N = \omega T_{\mathrm{r}} = \frac{cp_0LR\omega}{4} \int_{-1}^{1} \int_{0}^{\theta_{\mathrm{free}}} \left(H \frac{\partial P}{\partial \theta} + \frac{\Lambda}{3} \frac{1}{H}\right) \mathrm{d}\theta \mathrm{d}\lambda \tag{26}$$

Due to bearing symmetry in the axial direction, the side leakage flow rate of air is:

$$Q_{\mathrm{z}} = \frac{p_0c^3R}{3\mu\Re LT} \int_{0}^{\theta_{\mathrm{free}}} \left(PH^3 \frac{\partial P}{\partial \lambda}\right) \bigg|_{\lambda = 1} \mathrm{d}\theta \tag{27}$$

1.3 Calculation Model for Dynamic Performances

The criteria for measuring the dynamic performance of bump air foil bearings primarily involve dynamic stiffness and damping coefficients. Dynamic coefficients are calculated using perturbation methods. Air film pressure depends on rotor displacement and speed:

$$\begin{cases} F_{Nx} = F_{Nx}(x, y, x', y') = -\int_{-\frac{L}{2}}^{\frac{L}{2}} \int_{0}^{\theta_{\mathrm{free}}} P\sin\theta R \mathrm{d}\theta \mathrm{d}z \\ F_{Ny} = F_{Ny}(x, y, x', y') = \int_{-\frac{L}{2}}^{\frac{L}{2}} \int_{0}^{\theta_{\mathrm{free}}} P\cos\theta R \mathrm{d}\theta \mathrm{d}z \end{cases} \tag{28}$$

where F_{Nx}, F_{Ny} are air-film horizontal and vertical forces, respectively. x and y represent rotor's horizontal and vertical displacement, respectively. x' and y' denote its velocity components.

When the rotor is operating stably, perturbation displacements Δx and Δy, perturbation velocities $\Delta x'$ and $\Delta y'$ are applied to the rotor. The forces are in a Taylor series expansion:

$$\boldsymbol{F}_N = \begin{bmatrix} F_{Nx} \\ F_{Ny} \end{bmatrix} = \begin{bmatrix} F_{Nx0} \\ F_{Ny0} \end{bmatrix} + \frac{\partial \boldsymbol{F}_N}{\partial x}\bigg|_0 \Delta x + \frac{\partial \boldsymbol{F}_N}{\partial y'}\bigg|_0 \Delta y + \frac{\partial \boldsymbol{F}_N}{\partial x'}\bigg|_0 \Delta x' + \frac{\partial \boldsymbol{F}_N}{\partial y'}\bigg|_0 \Delta y' + O(\Delta x^2, \Delta y^2, \Delta x'^2, \Delta y'^2) \tag{29}$$

where the subscript "0" represents the quantity in the equilibrium position. Δx, Δy, $\Delta x'$, $\Delta y' \to 0$. Neglect the term $O(\Delta x^2, \Delta y^2, \Delta x'^2, \Delta y'^2)$, stiffness and damping coefficients are:

$$\begin{bmatrix} K_{xx} \\ K_{yx} \end{bmatrix} = \frac{\partial \boldsymbol{F}_N}{\partial x}\bigg|_0, \quad \begin{bmatrix} K_{xy} \\ K_{yy} \end{bmatrix} = \frac{\partial \boldsymbol{F}_N}{\partial y}\bigg|_0 \tag{30a}$$

$$\begin{bmatrix} C_{xx} \\ C_{yx} \end{bmatrix} = \frac{\partial \boldsymbol{F}_N}{\partial x'}\bigg|_0, \quad \begin{bmatrix} C_{xy} \\ C_{yy} \end{bmatrix} = \frac{\partial \boldsymbol{F}_N}{\partial y'}\bigg|_0 \tag{30b}$$

Then Eq. (29) is expressed as the matrix form:

$$\boldsymbol{F}_N = \begin{bmatrix} F_{Nx} \\ F_{Ny} \end{bmatrix} = \begin{bmatrix} F_{Nx0} \\ F_{Ny0} \end{bmatrix} + \boldsymbol{K}\begin{bmatrix} x \\ y \end{bmatrix} + \boldsymbol{C}\begin{bmatrix} x' \\ y' \end{bmatrix} \tag{31}$$

where $\boldsymbol{K}$, $\boldsymbol{C}$ are stiffness and damping matrices, respectively, and expressed as:

$$\boldsymbol{K} = \begin{bmatrix} K_{xx} & K_{xy} \\ K_{yx} & K_{yy} \end{bmatrix}, \boldsymbol{C} = \begin{bmatrix} C_{xx} & C_{xy} \\ C_{yx} & C_{yy} \end{bmatrix} \tag{32}$$

The dimensionless air film thickness and pressure, and total radial deformation of top foil are respectively written as: H_0, P_0, $\bar{w}_{\mathrm{t}0}$. The first-order Taylor series expansion of P, H, and $\bar{w}_{\mathrm{t}}$ ignoring the higher order quantities is:

$$\begin{cases} P = P_0 + P_x \overline{\Delta x} + P_{x'} \overline{\Delta x'} + P_y \overline{\Delta y} + P_{y'} \overline{\Delta y'} \\ H = H_0 + H_x \overline{\Delta x} + H_{x'} \overline{\Delta x'} + H_y \overline{\Delta y} + H_{y'} \overline{\Delta y'} \\ \bar{w}_{\mathrm{t}} = \bar{w}_{\mathrm{t}0} + \bar{w}_{\mathrm{t}x} \overline{\Delta x} + \bar{w}_{\mathrm{t}x'} \overline{\Delta x'} + \bar{w}_{\mathrm{t}y} \overline{\Delta y} + \\ \quad \bar{w}_{\mathrm{t}y'} \overline{\Delta y'} \end{cases} \tag{33}$$

where P_x, P_y, $P_{x'}$, $P_{y'}$ are pressure disturbances caused by Δx, Δy, $\Delta x'$, $\Delta y'$, respectively. H_x, H_y, $H_{x'}$, $H_{y'}$ are air film thickness disturbances caused by Δx, Δy, $\Delta x'$, $\Delta y'$, respectively. $\bar{w}_{\mathrm{t}x}$, $\bar{w}_{\mathrm{t}_y}$, $\bar{w}_{\mathrm{t}x'}$, $\bar{w}_{\mathrm{t}y'}$ are foil deflection disturbances caused by Δx, Δy, $\Delta x'$, $\Delta y'$, respectively.

Substituting Eq. (33) into Eq. (20), the perturbation pressure equations are as follows:

$$\frac{\partial}{\partial \theta}\left(P_x H_0^3 \frac{\partial P_0}{\partial \theta} + P_0 H_0^3 \frac{\partial P_x}{\partial \theta} + 3P_0 H_0^2 H_x \frac{\partial P_0}{\partial \theta}\right) + \left(\frac{2R}{L}\right)^2 \frac{\partial}{\partial \lambda}\left(P_x H_0^3 \frac{\partial P_0}{\partial \lambda} + P_0 H_0^3 \frac{\partial P_x}{\partial \lambda} + 3P_0 H_0^2 H_x \frac{\partial P_0}{\partial \lambda}\right) = \Lambda \frac{\partial}{\partial \theta}(P_0 H_x + P_x H_0) - 2v\Lambda(P_0 H_{x'} + P_{x'} H_0) \tag{34}$$

$$\frac{\partial}{\partial \theta}\left(P_{x'} H_0^3 \frac{\partial P_0}{\partial \theta} + P_0 H_0^3 \frac{\partial P_{x'}}{\partial \theta} + 3P_0 H_0^2 H_{x'} \frac{\partial P_0}{\partial \theta}\right) + \left(\frac{2R}{L}\right)^2 \frac{\partial}{\partial \lambda}\left(P_{x'} H_0^3 \frac{\partial P_0}{\partial \lambda} + P_0 H_0^3 \frac{\partial P_{x'}}{\partial \lambda} + 3P_0 H_0^2 H_{x'} \frac{\partial P_0}{\partial \lambda}\right) = \Lambda \frac{\partial}{\partial \theta}(P_0 H_{x'} + P_{x'} H_0) + 2v\Lambda(P_0 H_x + P_x H_0) \tag{35}$$

$$\frac{\partial}{\partial \theta}\left(P_y H_0^3 \frac{\partial P_0}{\partial \theta} + P_0 H_0^3 \frac{\partial P_y}{\partial \theta} + 3P_0 H_0^2 H_y \frac{\partial P_0}{\partial \theta}\right) +$$

$$\left(\frac{2R}{L}\right)^2 \frac{\partial}{\partial\lambda}\left(P_y H_0^3 \frac{\partial P_0}{\partial\lambda} + P_0 H_0^3 \frac{\partial P_y}{\partial\lambda} + 3P_0 H_0^2 H_y \frac{\partial P_0}{\partial\lambda}\right) =$$

$$\Lambda \frac{\partial}{\partial\theta}(P_0 H_y + P_y H_0) - 2v\Lambda(P_0 H_{y'} + P_{y'} H_0) \quad (36)$$

$$\frac{\partial}{\partial\theta}\left(P_{y'} H_0^3 \frac{\partial P_0}{\partial\theta} + P_0 H_0^3 \frac{\partial P_{y'}}{\partial\theta} + 3P_0 H_0^2 H_{y'} \frac{\partial P_0}{\partial\theta}\right) +$$

$$\left(\frac{2R}{L}\right)^2 \frac{\partial}{\partial\lambda}\left(P_{y'} H_0^3 \frac{\partial P_0}{\partial\lambda} + P_0 H_0^3 \frac{\partial P_{y'}}{\partial\lambda} + 3P_0 H_0^2 H_{y'} \frac{\partial P_0}{\partial\lambda}\right) =$$

$$\Lambda \frac{\partial}{\partial\theta}(P_0 H_{y'} + P_{y'} H_0) + 2v\Lambda(P_0 H_y + P_y H_0) \quad (37)$$

When the shaft is subjected to the above perturbations, H is expressed as follows:

$$H = H_0 + \overline{\Delta x}\sin(\theta+\beta) - \overline{\Delta y}\cos(\theta+\beta) +$$

$$\bar{w}_{tx}\overline{\Delta x} + \bar{w}_{tx'}\overline{\Delta x'} + \bar{w}_{ty}\overline{\Delta y} + \bar{w}_{ty'}\overline{\Delta y'} \quad (38)$$

Combining Eq. (38) with Eq. (33) yields:

$$\begin{cases} H_x = \bar{w}_{tx} + \sin(\theta+\beta), H_{x'} = \bar{w}_{tx'} \\ H_y = \bar{w}_{ty} - \cos(\theta+\beta), H_{y'} = \bar{w}_{ty'} \end{cases} \quad (39)$$

By substituting Eq. (39) into Eqs. (34)-(37), the air film pressure P_x, $P_{x'}$, P_y, and $P_{y'}$ can be obtained. Then, dynamic performance coefficients are:

$$\begin{bmatrix} K_{xx} & K_{xy} \\ K_{yx} & K_{yy} \end{bmatrix} = \frac{p_0 RL}{2c} \int_{-1}^{1} \int_{0}^{\theta_{\text{free}} + \sum_1^m \xi_i^{(k)}}$$

$$\begin{bmatrix} -P_x\sin(\theta+\beta) & -P_y\sin(\theta+\beta) \\ P_x\cos(\theta+\beta) & P_y\cos(\theta+\beta) \end{bmatrix} \mathrm{d}\theta\mathrm{d}\lambda \quad (40)$$

$$\begin{bmatrix} C_{xx} & C_{xy} \\ C_{yx} & C_{yy} \end{bmatrix} = \frac{p_0 RL}{2c\omega_e} \int_{-1}^{1} \int_{0}^{\theta_{\text{free}} + \sum_1^m \xi_i^{(k)}}$$

$$\begin{bmatrix} -P_{x'}\sin(\theta+\beta) & -P_{y'}\sin(\theta+\beta) \\ P_{x'}\cos(\theta+\beta) & P_{y'}\cos(\theta+\beta) \end{bmatrix} \mathrm{d}\theta\mathrm{d}\lambda \quad (41)$$

The boundary conditions of dimensionless pressure during the solution of dynamic performance coefficients are as follows:

$$\begin{cases} P_x(0,\lambda) = 0, P_x(\theta_{\text{free}},\lambda) = 0, P_x(\theta,\lambda = \pm 1) = 0 \\ P_{x'}(0,\lambda) = 0, P_{x'}(\theta_{\text{free}},\lambda) = 0, P_{x'}(\theta,\lambda = \pm 1) = 0 \\ P_y(0,\lambda) = 0, P_y(\theta_{\text{free}},\lambda) = 0, P_y(\theta,\lambda = \pm 1) = 0 \\ P_{y'}(0,\lambda) = 0, P_{y'}(\theta_{\text{free}},\lambda) = 0, P_{y'}(\theta,\lambda = \pm 1) = 0 \end{cases} \quad (42)$$

1.4 Numerical Calculation Method

In this study, the dimensionless Reynolds equation is solved using the finite difference method with iterative point-by-point convergence. As shown in Fig. 5, the load area is gridded circumferentially and axially. The area between adjacent bumps is divided into X parts. The initial step length of each grid is equal, which can be expressed as follows:

$$\Delta\theta_i^{(1)} = \frac{s}{XR} \quad (43)$$

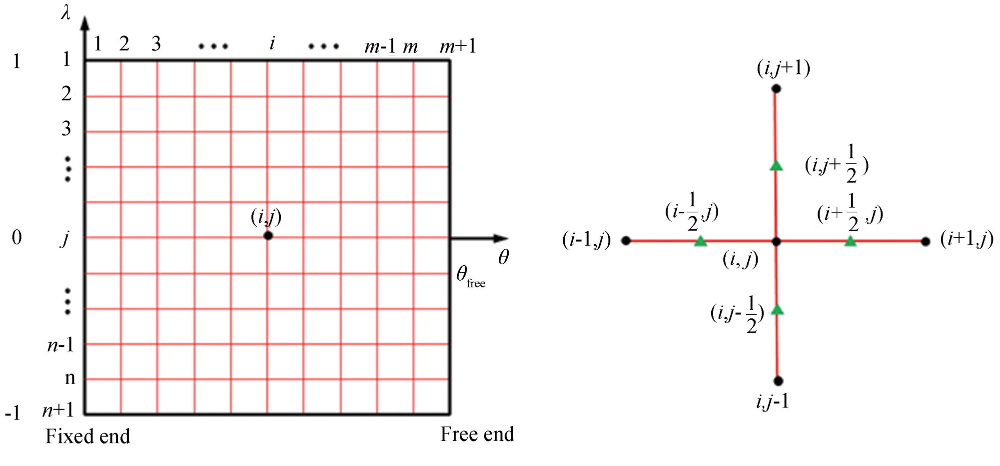

Fig.5 Schematic of mesh and difference quotient

Starting from the second iteration, the grid step length in the circumferential direction of foils changes with deformation. Therefore, during k-th iteration, the grid step length can be expressed as follows:

$$\Delta\theta_i^{(k)} = \frac{s}{XR} + \xi_i^{(k)} \quad (44)$$

where $\xi_i^{(k)}$ represents the change in the i-th grid in the circumferential direction during the k-th iteration.

In the axial direction, the grid step length does not change with the number of iterations. Therefore, it can be expressed as follows:

$$\Delta\lambda = \frac{2}{n} \quad (45)$$

The high-precision central difference quotient is used to replace the partial derivative terms. The convergence criteria for air film pressure and load capacity are:

$$\mathrm{Error}_P=\frac{\sum\limits_{j=1}^{n+1}\sum\limits_{i=1}^{m+1}\left|P_{i,j}^{(k)}-P_{i,j}^{(k-1)}\right|}{\sum\limits_{j=1}^{n+1}\sum\limits_{i=1}^{m+1}\left|P_{i,j}^{(k)}\right|}\leqslant 10^{-5}\qquad(46)$$

$$\mathrm{Error}_W=\frac{\left|W^{(k)}-W^{(k-1)}\right|}{W^{(k)}}\leqslant 10^{-5}\qquad(47)$$

The convergence criteria for the calculation of the dynamic performance are:

$$\mathrm{Error}_{P_x}=\frac{\sum\limits_{j=1}^{n+1}\sum\limits_{i=1}^{m+1}\left|(P_x)_{i,j}^{(k)}-(P_x)_{i,j}^{(k-1)}\right|+\sum\limits_{j=1}^{n+1}\sum\limits_{i=1}^{m+1}\left|(P_{x'})_{i,j}^{(k)}-(P_{x'})_{i,j}^{(k-1)}\right|}{\sum\limits_{j=1}^{n+1}\sum\limits_{i=1}^{m+1}\left|(P_x)_{i,j}^{(k)}\right|+\sum\limits_{j=1}^{n+1}\sum\limits_{i=1}^{m+1}\left|(P_{x'})_{i,j}^{(k)}\right|}\leqslant 10^{-5}\qquad(48)$$

$$\mathrm{Error}_{P_y}=\frac{\sum\limits_{j=1}^{n+1}\sum\limits_{i=1}^{m+1}\left|(P_y)_{i,j}^{(k)}-(P_y)_{i,j}^{(k-1)}\right|+\sum\limits_{j=1}^{n+1}\sum\limits_{i=1}^{m+1}\left|(P_{y'})_{i,j}^{(k)}-(P_{y'})_{i,j}^{(k-1)}\right|}{\sum\limits_{j=1}^{n+1}\sum\limits_{i=1}^{m+1}\left|(P_y)_{i,j}^{(k)}\right|+\sum\limits_{j=1}^{n+1}\sum\limits_{i=1}^{m+1}\left|(P_{y'})_{i,j}^{(k)}\right|}\leqslant 10^{-5}\qquad(49)$$

2 Results and Discussion

2.1 Experimental Verification

As shown in Fig. 6, the friction torque of the bearing was measured on a bearing test rig developed in our laboratory. The bearing basic parameters are shown in Table 1.

The experiments were conducted at 26 ℃ whith a rotational speed of $n=$ 20000 r/min. Friction torque T_{r} is measured with different radial clearances c and loads W during stable operation.

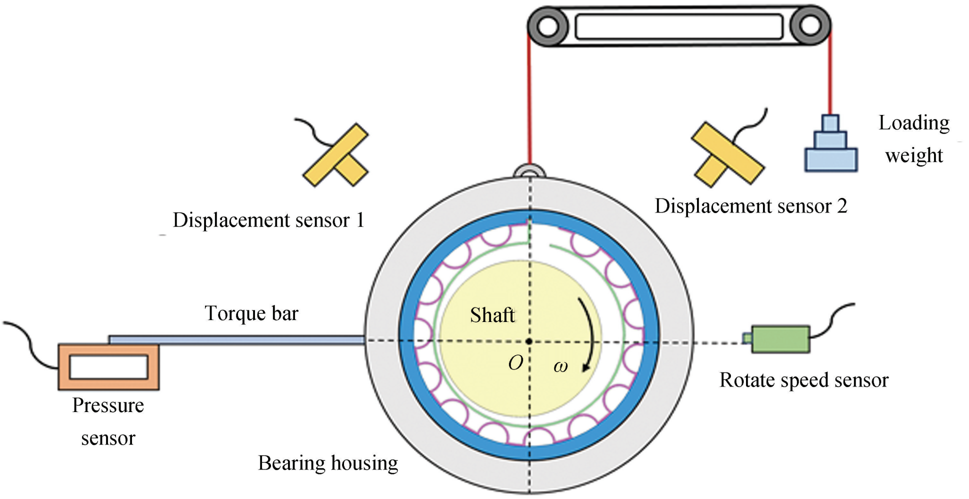

(a) The measuring mechanism

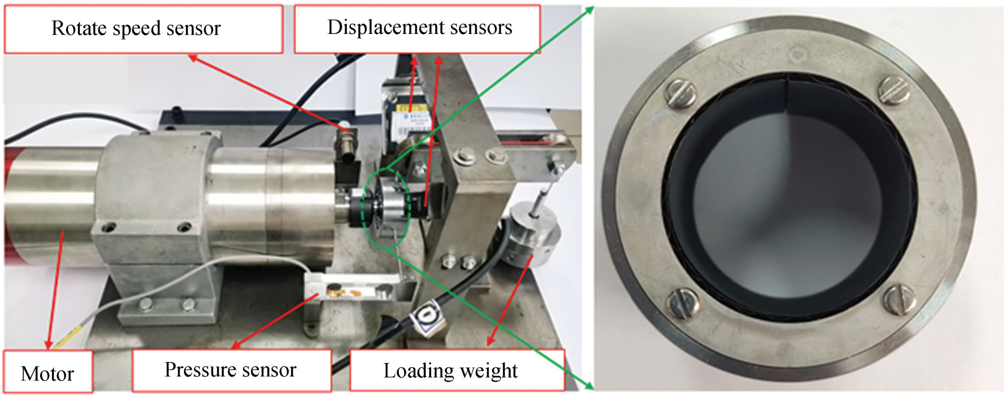

(b) The test rig

(c) The test bearing

Fig.6 Bump air foil bearing test rig

Every experimental datum represents the average of five measurements. The comparative results of experiments and numerical simulations are shown in Fig.7. It can be seen that the friction torque T_r decreases gradually with radial clearance c, which varies within the range of 105-255 μm when the load W=5 N. T_r increases with W, which varies within the range of 3.5-5.5 N when the radial clearance c = 210 μm. Consistent experimental and numerical results demonstrate the reliability of the theoretical model.

Table 1 Basic parameters of the bearing

Modulus of elasticity E (N/m^2)	Ambient atmospheric pressure p_0(Pa)	Foil proportional damping coefficient ζ [33-34]	Poisson's ratio u_b	Top foil thickness t_t(mm)	Bump foil thickness t_b(mm)	Bump arch half-length l (mm)
2.06×10^{11}	101325	0.2	0.3	0.1	0.07	1.7
Bump distance of bump foil s (mm)	Dynamic viscosity of air at 26 ℃ μ(mPa · s)	The eccentricity of bearing ε	Bearing width L (mm)	Bearing inner diameter R (mm)	Bump arch radius R_0(mm)	
4.2	0.01932	0.9	25	14.5	3.2	

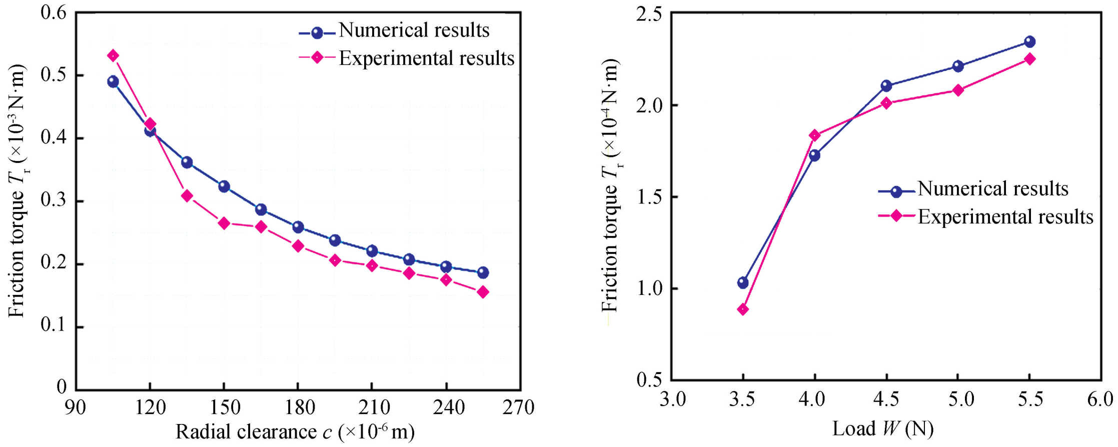

(a) Friction torque versus radial clearance (b) Friction torque versus with load

Fig.7 Variation of friction torque with radial clearance and load

2.2 Influences of Radial Clearance on Lubrication Performances

After verifying the calculation model established in this study by experiments, the performance of the bump foil bearing was numerically studied. Based on the theoretical model established above, the dimensionless air film pressure and thickness distributions were first calculated when n=50000 r/min, c=30 μm, and W=5 N (as shown in Fig. 8).

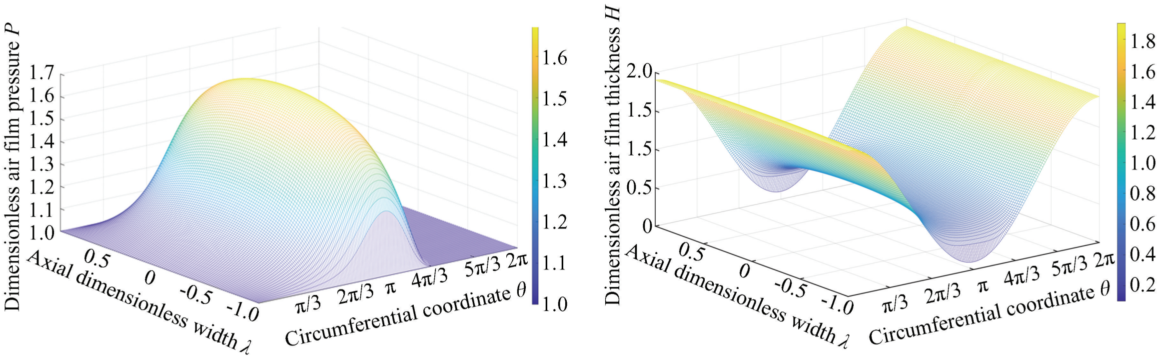

(a) Dimensionless air film pressure (b) Dimensionless air film thickness

Fig. 8 Dimensionless air film pressure and thickness distribution of bump air foil bearing

The results in Fig. 9 and Fig. 10 are calculated at the middle plane ($\lambda = 0$) of the bearing when load $W=5$ N. Fig. 9 demonstrates radial clearance effects on dimensionless air film pressure and thickness when $n=50000$ r/min. Fig. 10 shows the relationship of the maximum air film pressure $P_{\max}$ and the minimum air film thickness $H_{\min}$ with radial clearance under different rotational speeds when $W=5$ N. It can be seen that $P_{\max}$ increases with radial clearance but decreases with rotational speed, while $H_{\min}$ decreases with radial clearance and increases with rotational speed.

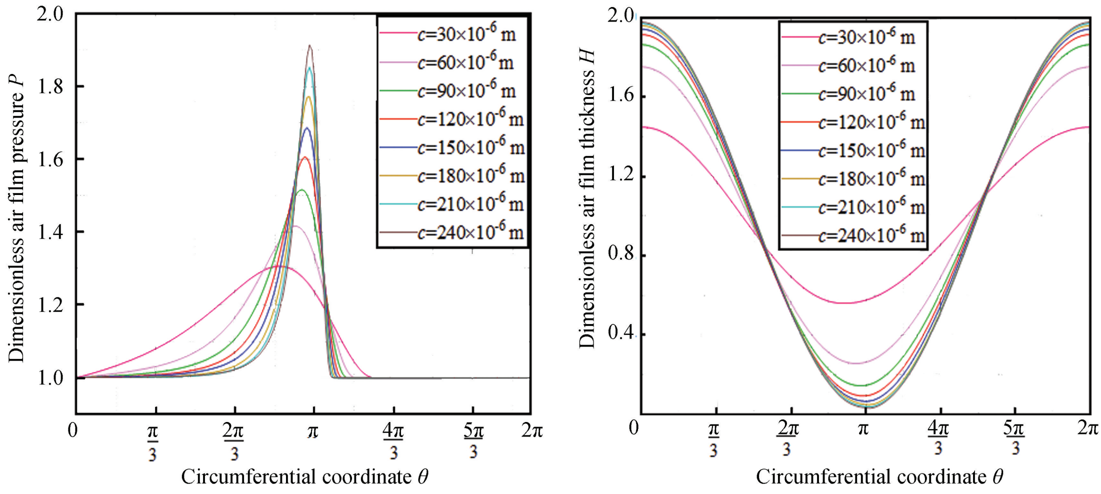

(a) The film pressure

(b) The film thickness

Fig.9 Dimensionless air film pressure and thickness distribution

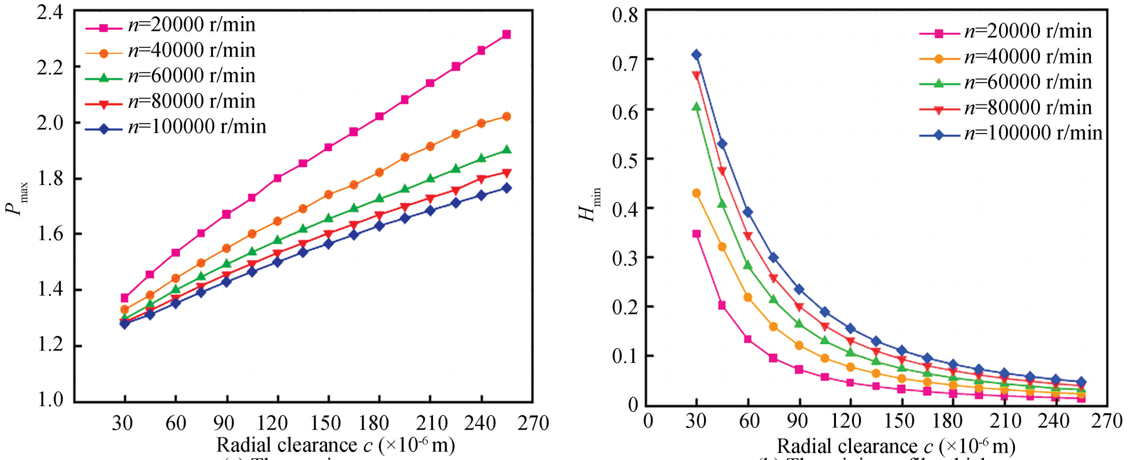

(a) The maximun pressure

(b) The minimun film thickness

Fig.10 Dimensionless maximum air film pressure and minimum air film thickness versus radial clearance

Localized contact between rotor and bearing inner surfaces occurs when the minimum air film thickness is less than the roughness of the two surfaces, which result in bearing failure. Therefore, the maximum load capacity refers to the capacity when the minimum air film thickness is 2 μm[35]. Fig. 11 (a) shows the maximum load capacity $W_{\max}$ versus radial clearance. It can be seen that $W_{\max}$ decreases with radial clearance but increases with rotational speed.

Figs. 11 (b)−(d) show that the friction torque T_r, friction power loss N and side leakage flow rate of gas Q_z versus the radial clearance under different rotational speeds when the load $W=5$ N. It can be known that T_r and N increase with rotational speed and decrease with radial clearance. Q_z increases with radial clearance. The reason is that the effective area of the side leakage flow rate increases with radial clearance.

2.3 Influences of Foils Structural Parameters on Lubrication Performances

The influences of foils' structural parameters on bearing lubrication performance were investigated at $n=50000$ r/min. Using the control variable method, all other parameters remained consistent with Table 1 while changing one parameter at a time. The maximum load capacity $W_{\max}$ is calculated when $H_{\min} = 2$ μm. Friction torque T_r, friction power loss N and side leakage flow rate of gas Q_z are calculated for a given load $W = 5$ N.

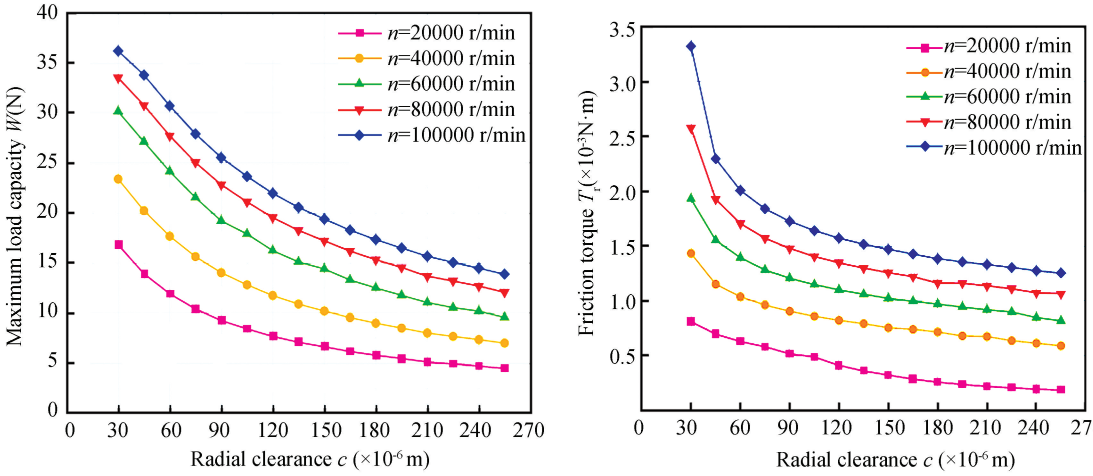

(a) The maximum load capacity

(b) The friction torque

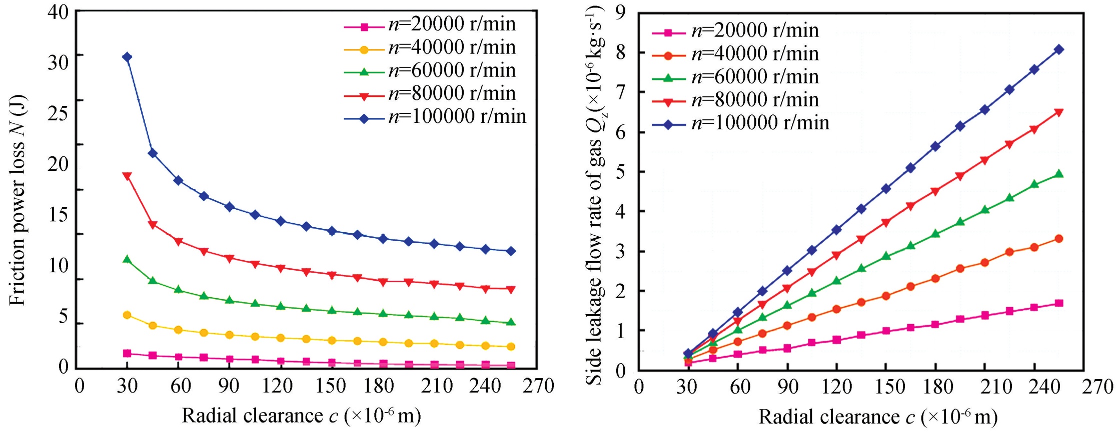

(c) The friction power loss

(d) The side leakage flow rate of gas

Fig.11 The lubrication performances versus radial clearance

Fig. 12 shows the variation of $W_{\max}$, T_r, N and Q_z with top foil thickness t_t under different radial clearances. It can be seen that $W_{\max}$ increases with t_t. T_r and N increase with t_t. However, the increasing trend is no longer obvious when t_t is greater than 0.11×10^{-3} m. Q_z presents a significant increase with t_t at large radial clearance.

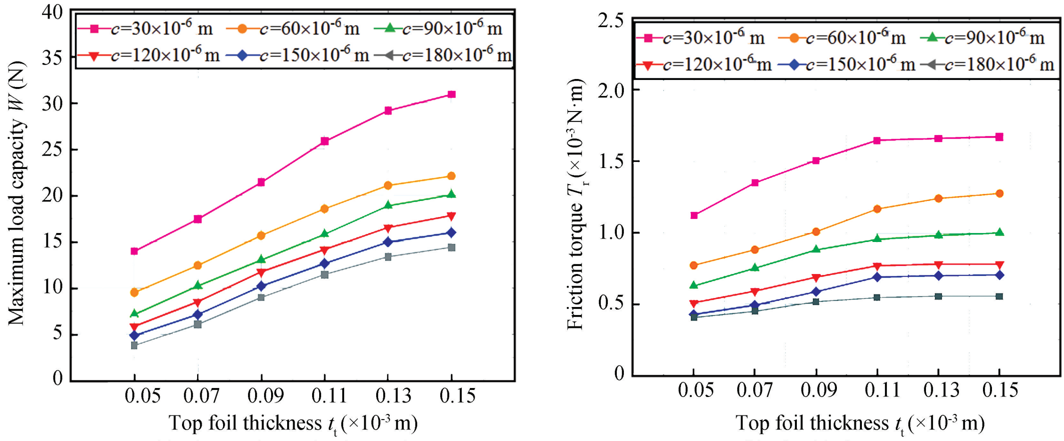

(a) The maximum load capacity

(b) The friction torque

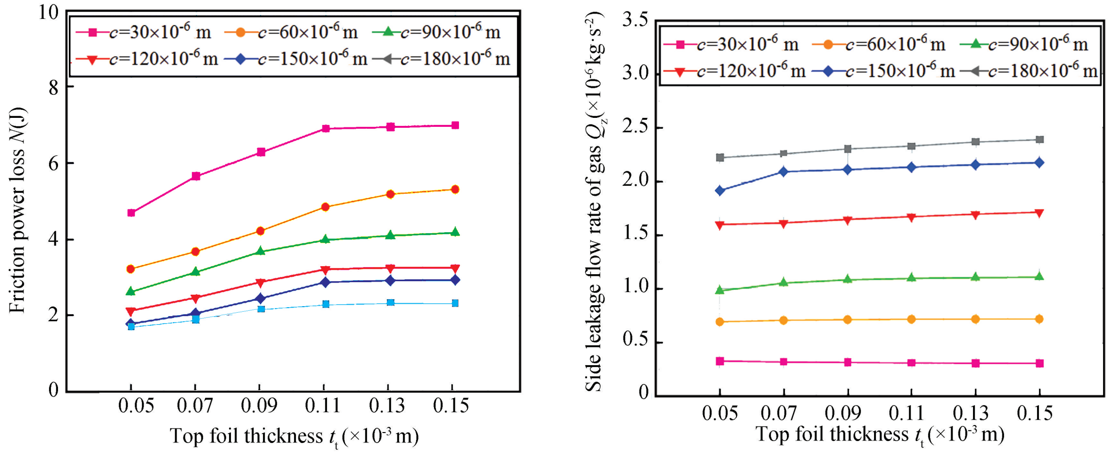

(c) The friction power loss

(d) The side leakage flow rate of gas

Fig.12 The lubrication performances versus top foil thickness

Fig. 13 shows the variation of $W_{\max}$, T_r, N and Q_z with bump foil thickness t_b under different radial clearances. It can be known that $W_{\max}$, T_r, N increase with t_b and the increasing trend is more significant with smaller radial clearance. Q_z presents a significant increase with t_b at larger radial clearance.

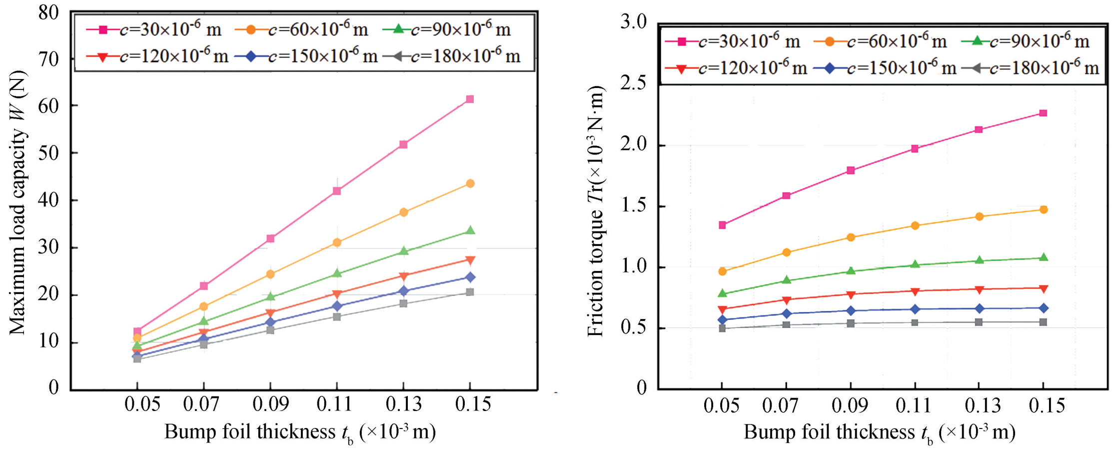

(a) The maximum load capacity

(b) The friction torque

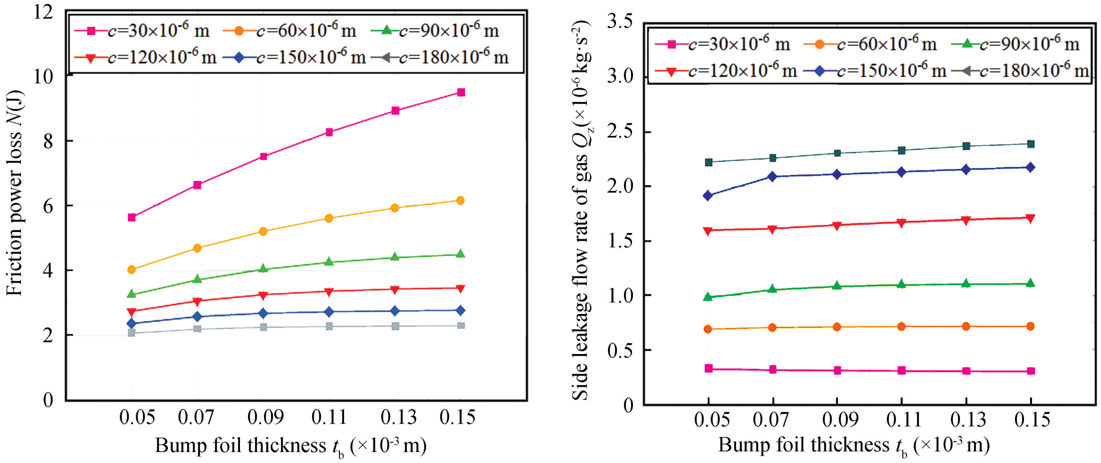

(c) The friction power loss

(d) The side leakage flow rate of gas

Fig.13 The lubrication performances versus bump foil thickness

Fig.14 shows the variation of $W_{\max}$, T_r, N and Q_z with bump arch half-length l under different radial clearances. It can be known that $W_{\max}$, T_r, N decrease with l and the decreasing trend is more significant with smaller radial clearance. Q_z presents a significant decrease trend as l increases at larger radial clearance. Fig.15 shows the variation of $W_{\max}$, T_r, N and Q_z with bump arch radius R_0 under different radial clearances. It can be seen that $W_{\max}$, T_r, N and Q_z do not change significantly with R_0.

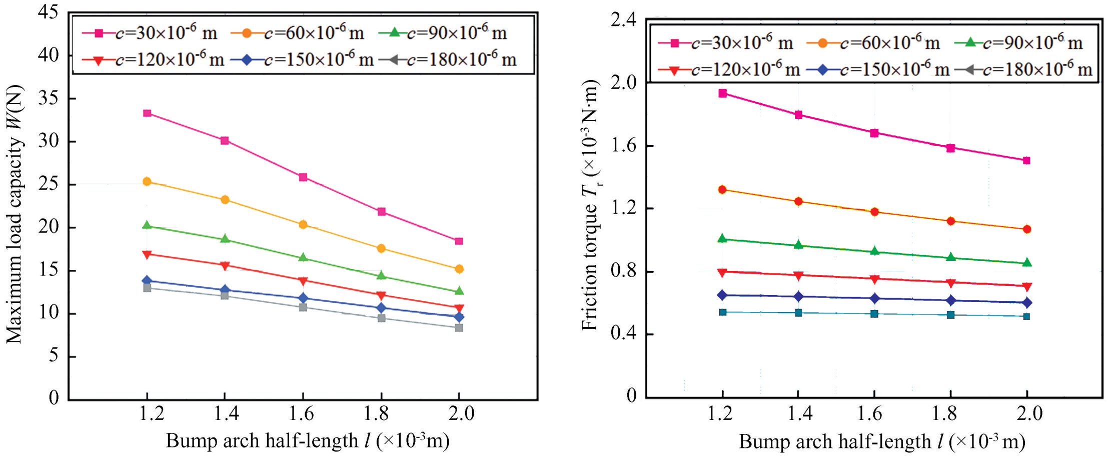

(a) The maximum load capacity (b) The friction torque

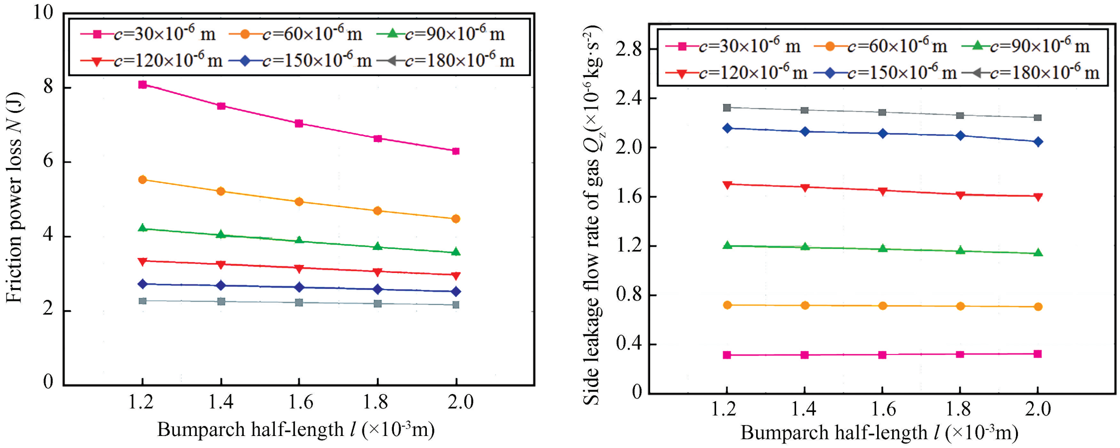

(c) The friction power loss (d) The side leakage flow rate of gas

Fig.14 The lubrication performances versus bump arch half-length

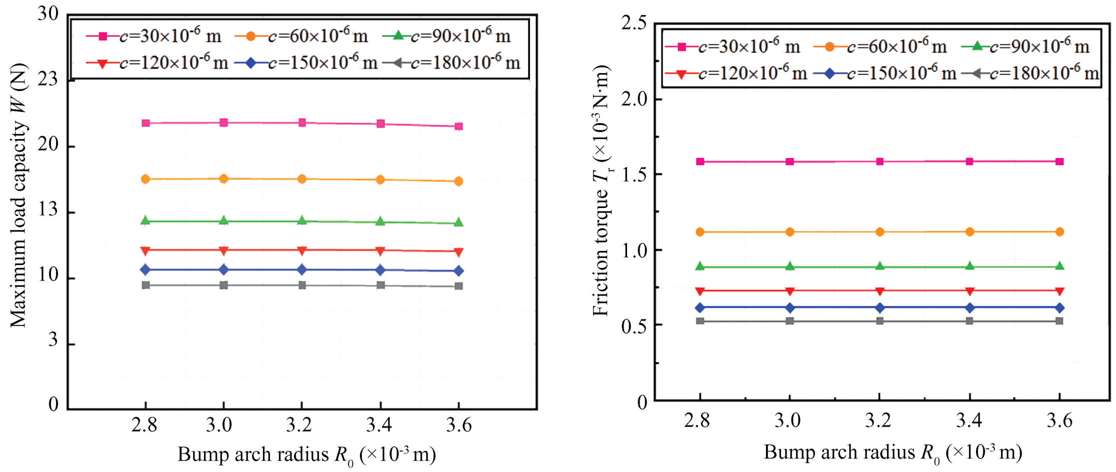

(a) The maximum load capacity (b) The friction torque

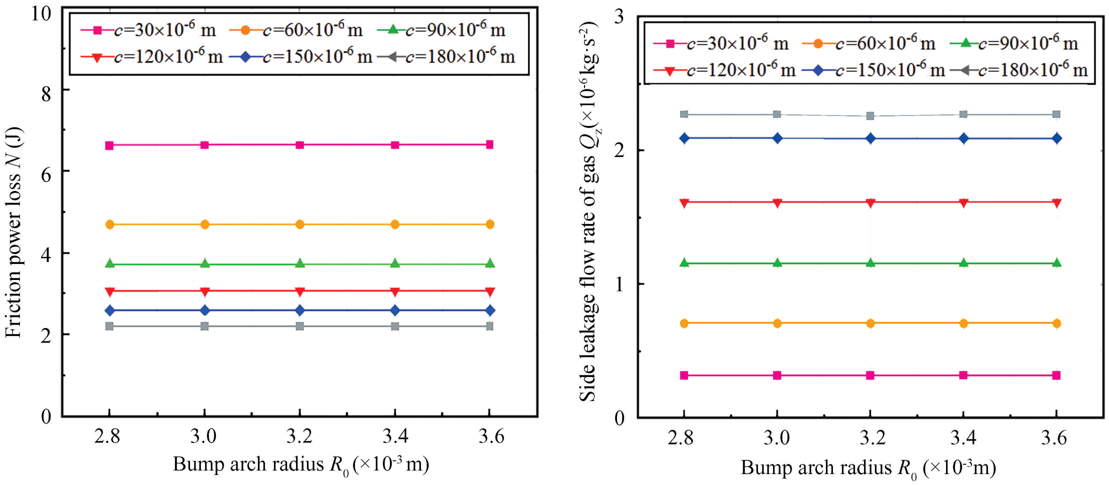

(c) The friction power loss

(d) The side leakage flow rate of gas

Fig.15 The lubrication performances versus bump arch radius

2.4 Influences of Radial Clearance on Dynamic Performances

Utilizing the dynamic calculation model of bearings established in this study and the parameters in Table 1, the dynamic performance coefficients with radial clearance c under different rotational speeds were calculated when the whirl frequency ratio $v = 1$ of the rotor and the load $W = 5$ N.

Fig. 16 shows that K_{xx} and K_{yy} decrease with radial clearance but increase with rotational speed. The result echoes the situation where $W_{\max}$ varies with the radial clearance, i. e. when the radial clearance becomes large, $W_{\max}$ approaches zero, so the main stiffness coefficients also approach zero.

The cross-stiffness coefficient K_{xy} peaks before declining toward zero with radial clearance, while increasing with rotational speed. K_{yx} initially increases and then decreases with rotational speed, and initially decreases and then increases toward zero with radial clearance. Fig. 17 reveals decreasing C_{xx} and C_{yy} with larger radial clearance and higher rotational speed. C_{xy} increases with radial clearance and gradually approaches zero. C_{yx} decreases and then increases towar d zero with radial clearance.

2.5 Influences of Foils' Structural Parameters on Dynamic Performances

The dynamic coefficients versus structural parameters of foils at different radial clearances were calculated when $W = 5$ N.

Fig.18 demonstrates that dynamic stiffness coefficients versus top foil thickness t_{t} . K_{xx} and K_{yy} increase as t_{t} increases, and the increasing trend becomes more significant with smaller radial clearances. K_{xy} initially decreases and then increases as t_{t} increases. K_{yx} decreases with t_{t} .

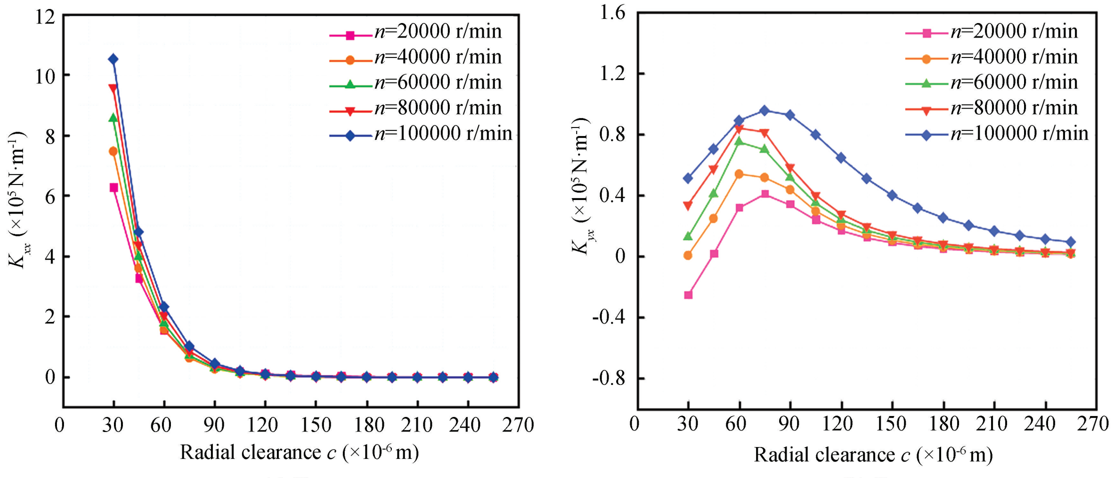

(a) K_{xx}

(b) K_{xy}

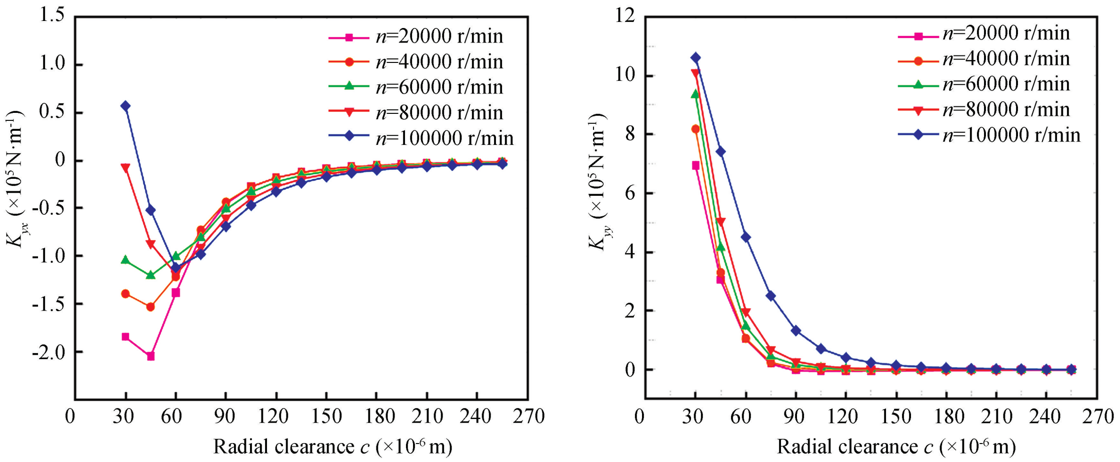

(c) K_{yx} (d) K_{yy}

Fig.16 Stiffness coefficients versus radial clearance

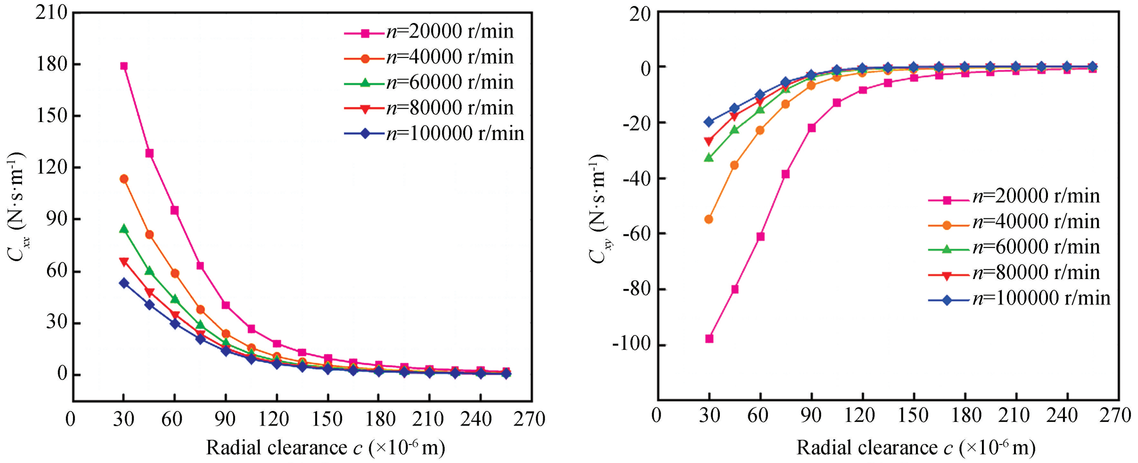

(a) C_{xx} (b) C_{xy}

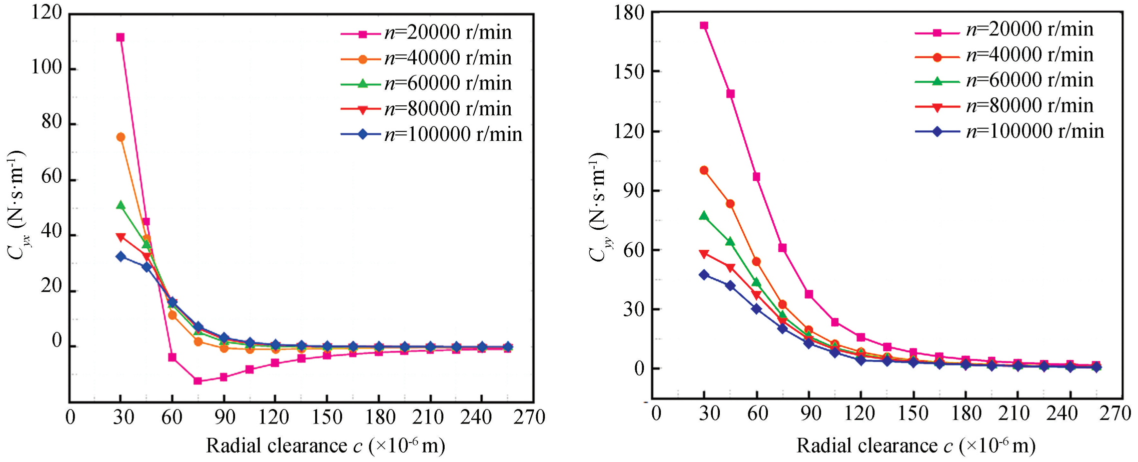

(c) C_{yx} (d) C_{yy}

Fig.17 Damping coefficients versus radial clearance

Fig.19 demonstrates that dynamic damping coefficients versus t_t under different radial clearances. C_{xx} and C_{yy} increase as t_t increases. However, C_{xy} and C_{yx} decrease with t_t.

Fig.20 shows that the dynamic stiffness coefficients versus bump foil thickness t_b. K_{xx} and K_{yy}

and K_{xy} increase as t_b increases, and the influence is more significant with smaller radial clearances. K_{yx} decreases with t_b .

Fig.21 demonstrates that dynamic damping coefficients versus t_b under different radial clearances. It can be seen that C_{xx} , C_{yy} , C_{xy} and C_{yx} increase as t_b increases.

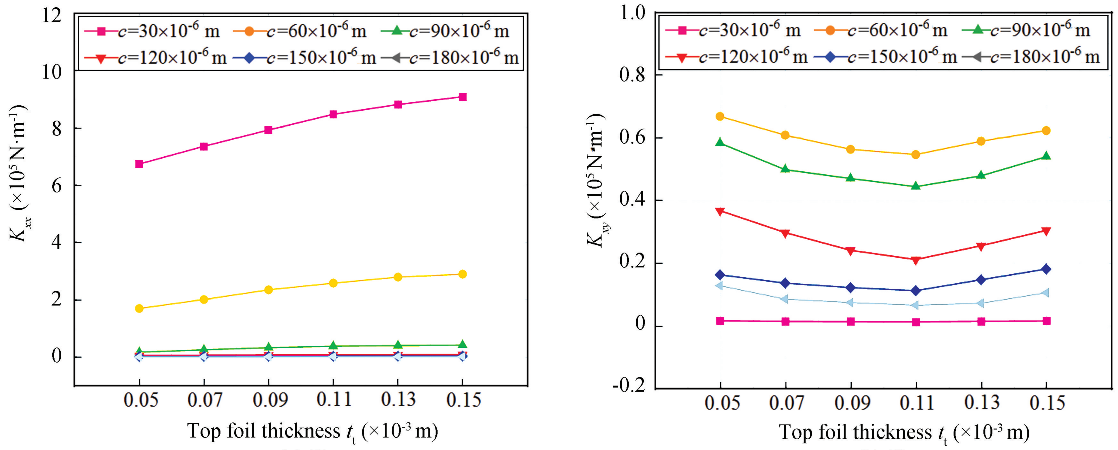

(a) K_{xx}

(b) K_{xy}

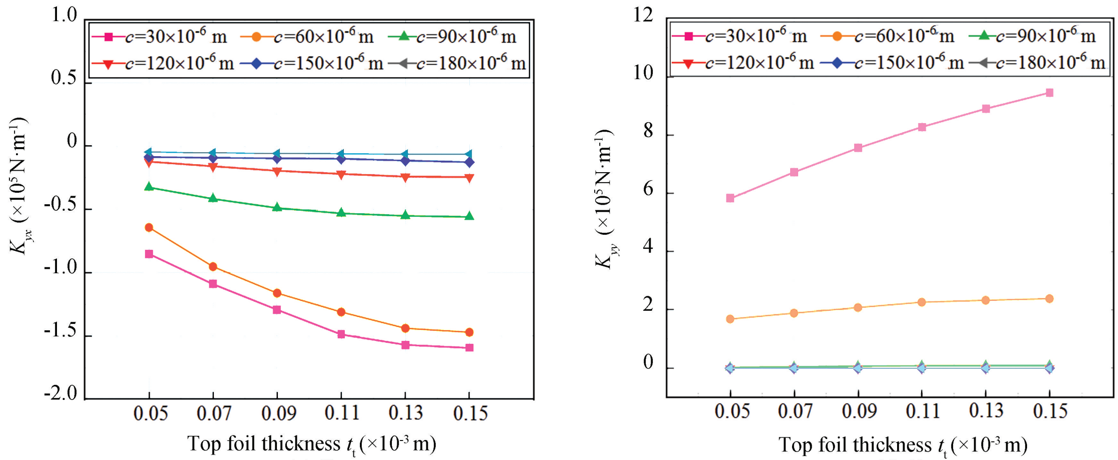

(c) K_{yx}

(d) K_{yy}

Fig.18 Stiffness coefficients versus top foil thickness

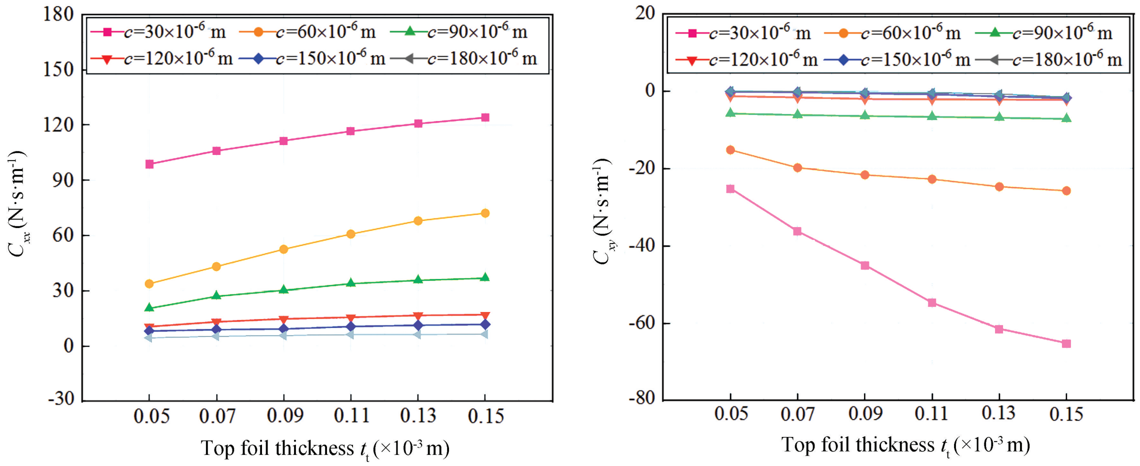

(a) C_{xx}

(b) C_{xy}

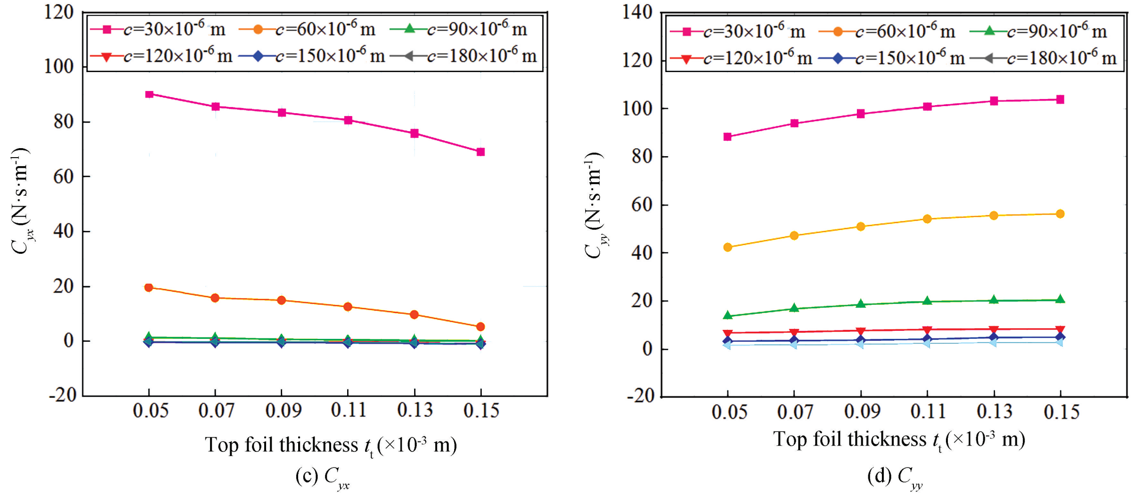

(c) C_{yx} (d) C_{yy}

Fig.19 Damping coefficients versus top foil thickness

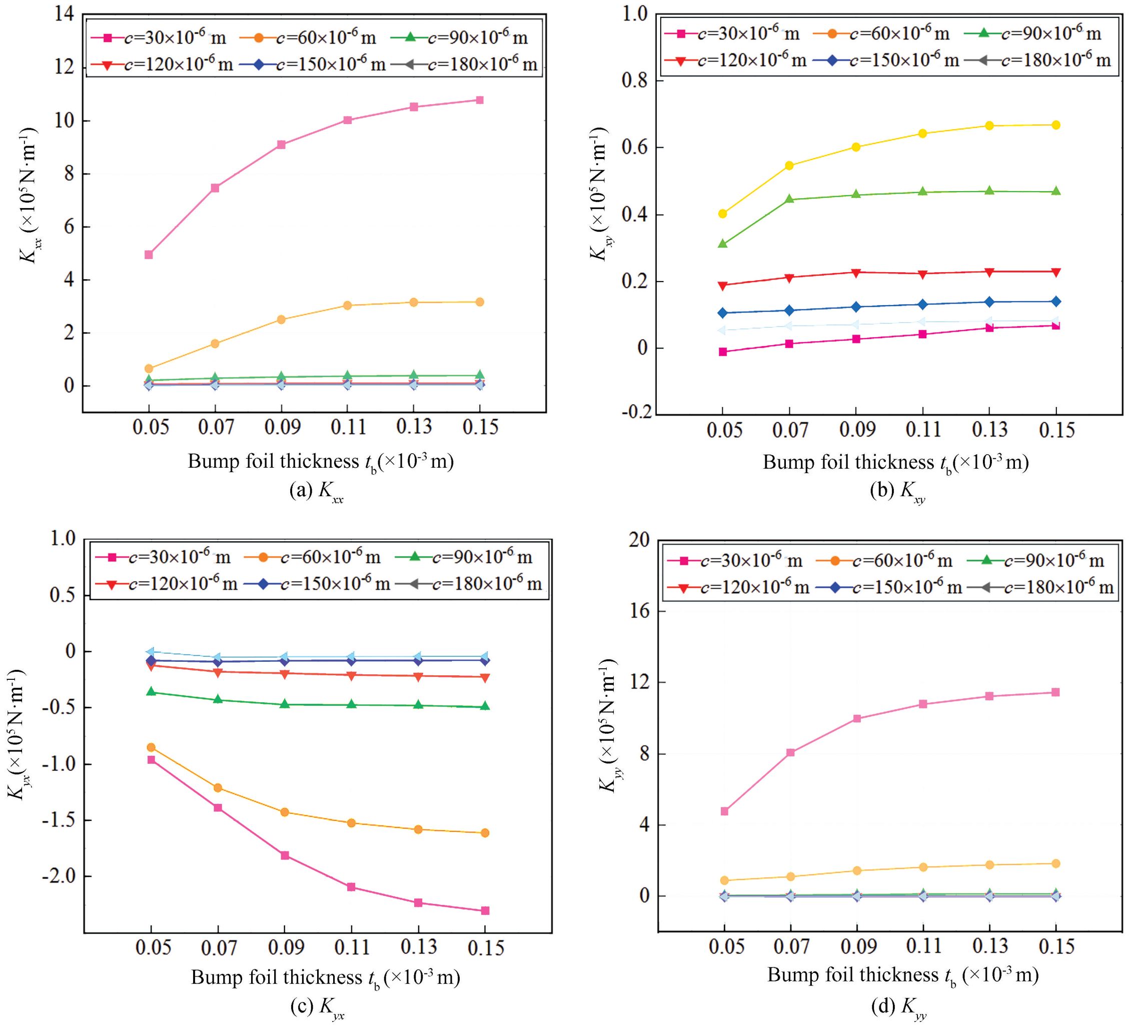

(a) K_{xx} (b) K_{xy}

(c) K_{yx} (d) K_{yy}

Fig.20 Stiffness coefficients versus bump foil thickness

Fig.22 demonstrates how dynamic stiffness coefficients change with bump arch half-length l across different radial clearances. K_{xx} and K_{yy} increase as l increases, and the increasing trend becomes more significant with smaller radial clearances. K_{xy} decreases with l, but K_{yx} varies insignificantly.

Fig. 23 demonstrates that dynamic damping coefficients versus l under different radial clearances. It can be seen that C_{xx}, C_{yy}, C_{xy} and C_{yx} decrease as l increases.

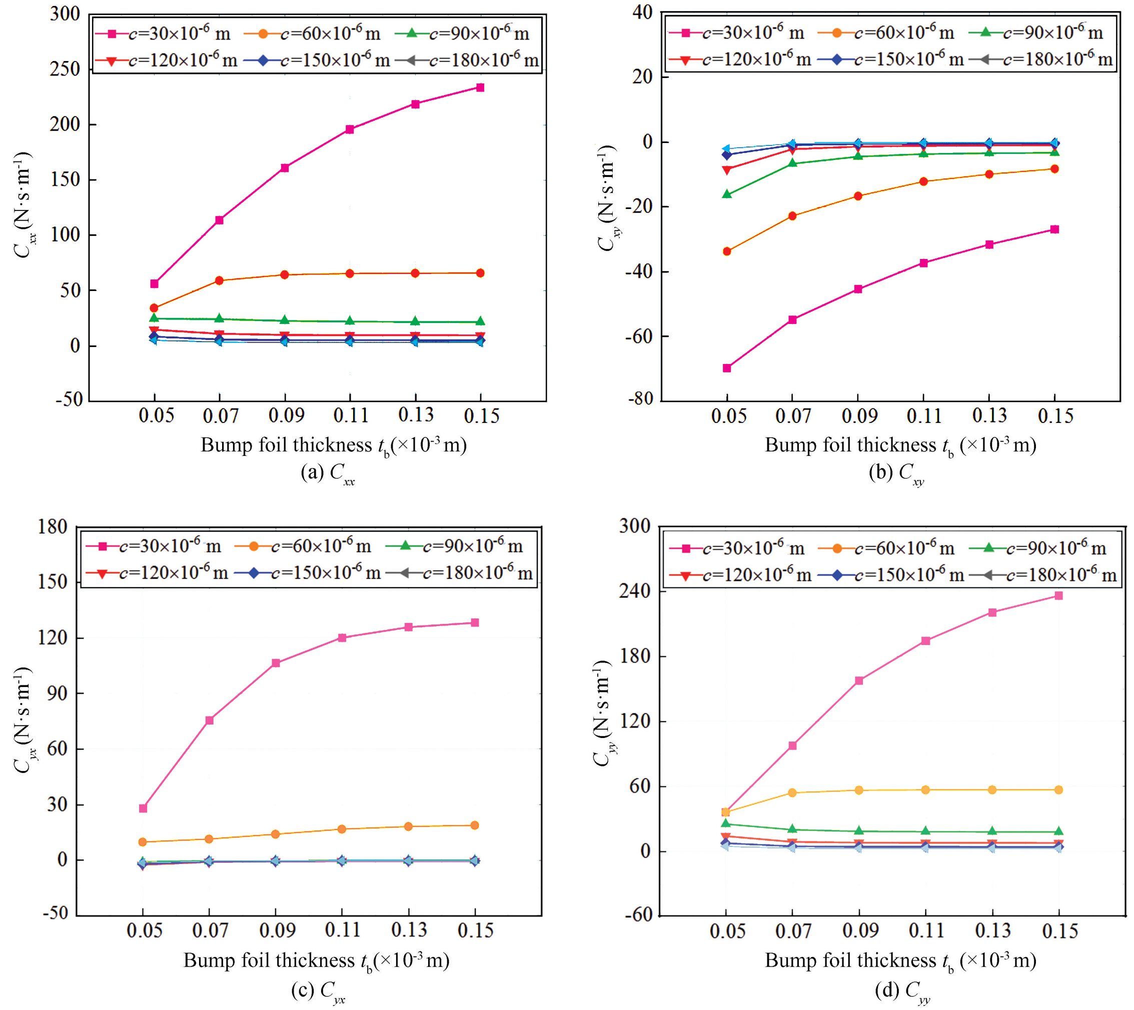

(a) C_{xx} (b) C_{xy}

(c) C_{yx} (d) C_{yy}

Fig.21 Damping coefficients versus bump foil thickness

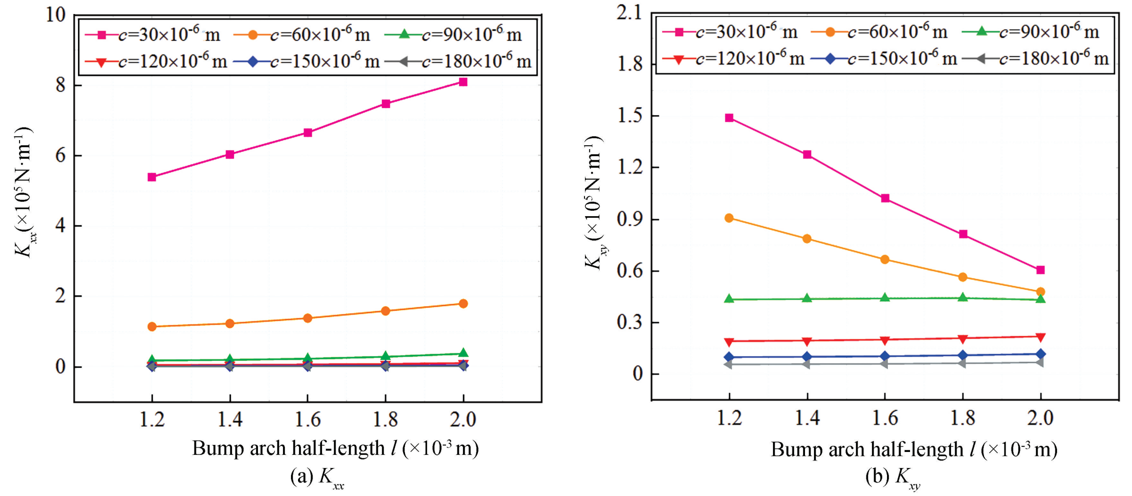

(a) K_{xx} (b) K_{xy}

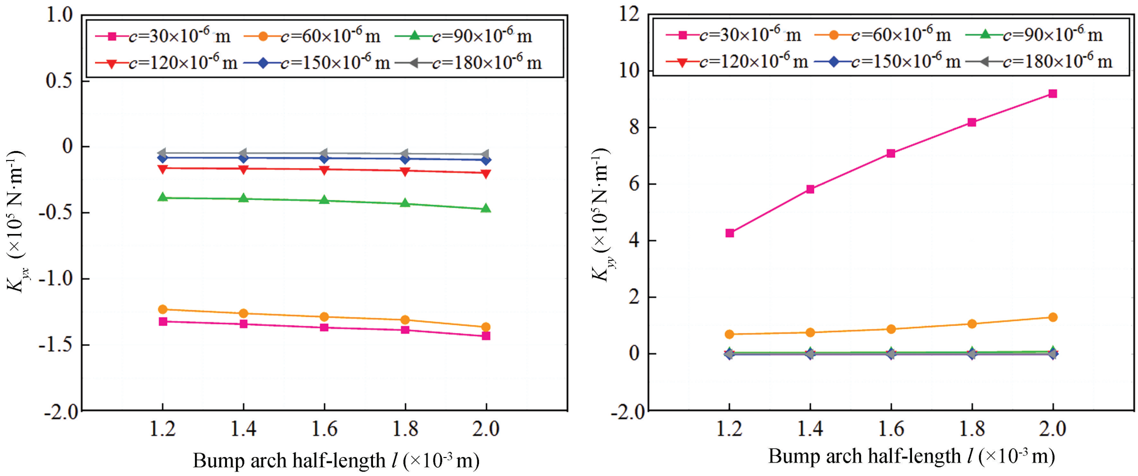

(c) K_{yx} (d) K_{yy}

Fig.22 Stiffness coefficients versus bump arch half-length

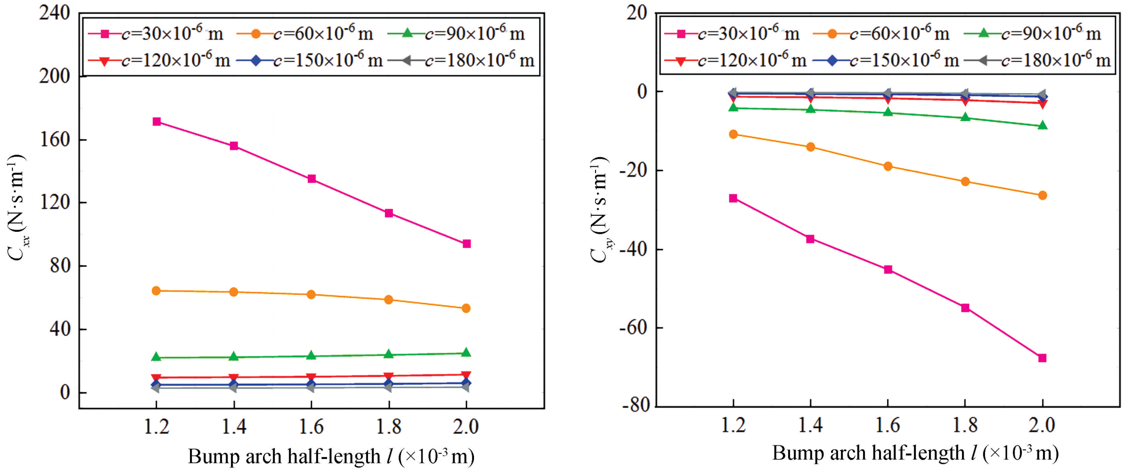

(a) C_{xx} (b) C_{xy}

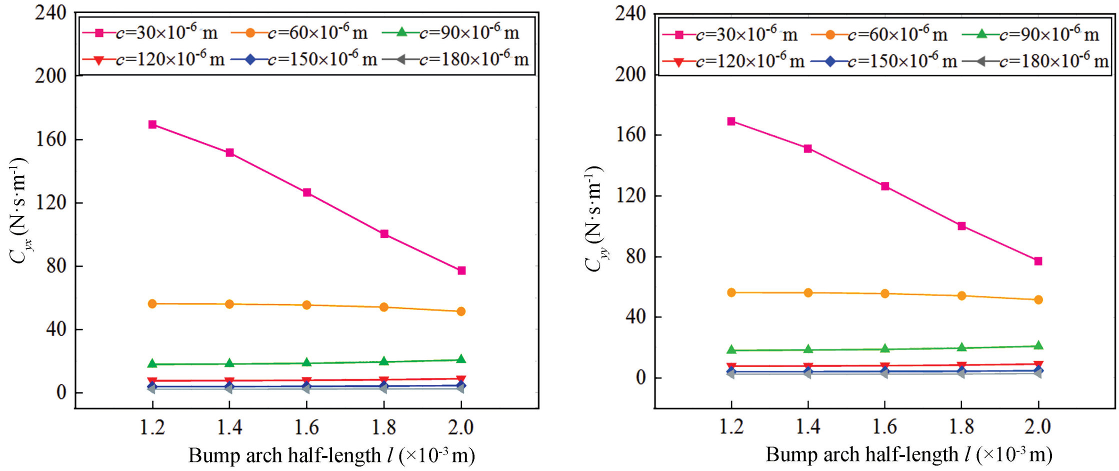

(c) C_{yx} (d) C_{yy}

Fig. 23 Damping coefficients versus bump arch half-length

Fig.24 and Fig.25 present dynamic stiffness and damping coefficients versus bump arch radius R_0 under different radial clearances, respectively. All eight coefficients change slightly with R_0.

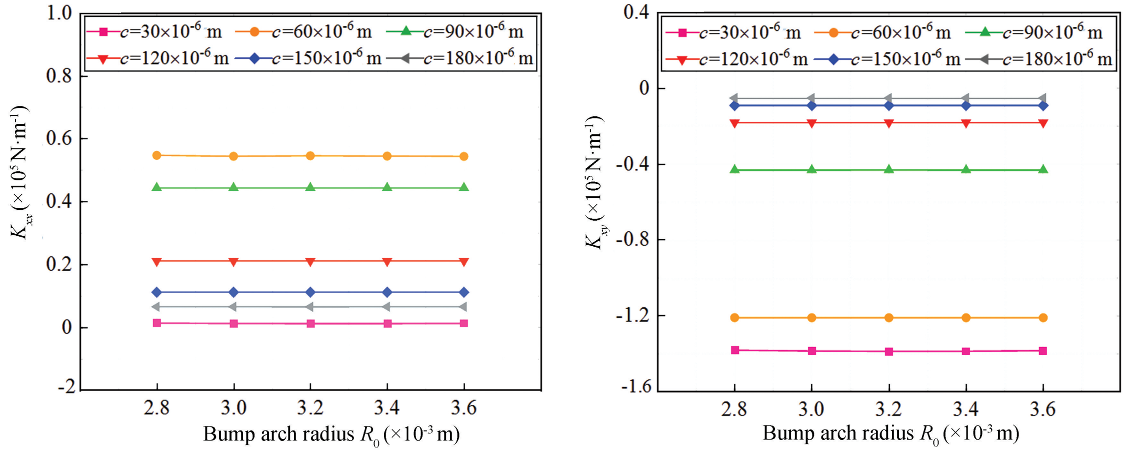

(a) K_{xx} (b) K_{xy}

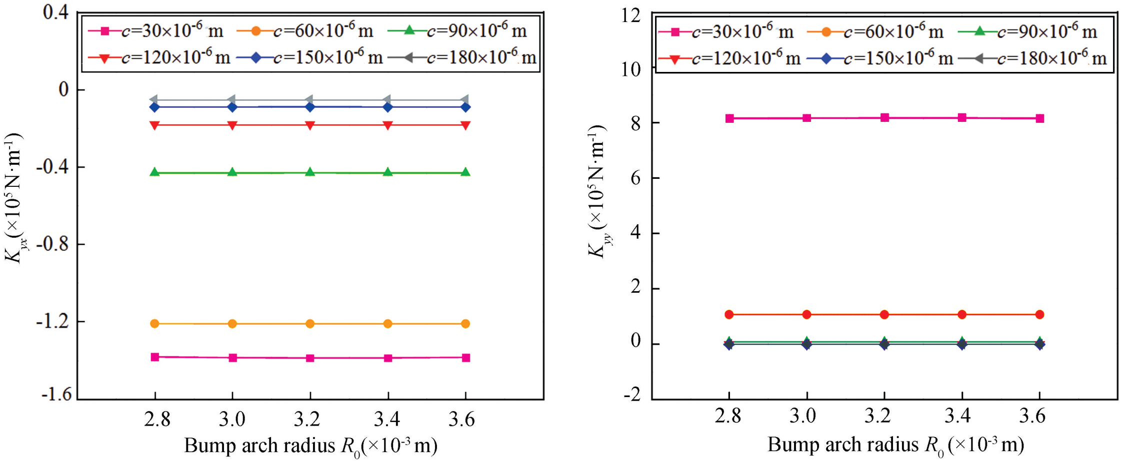

(c) K_{yx} (d) K_{yy}

Fig.24 Stiffness coefficients versus bump arch radius

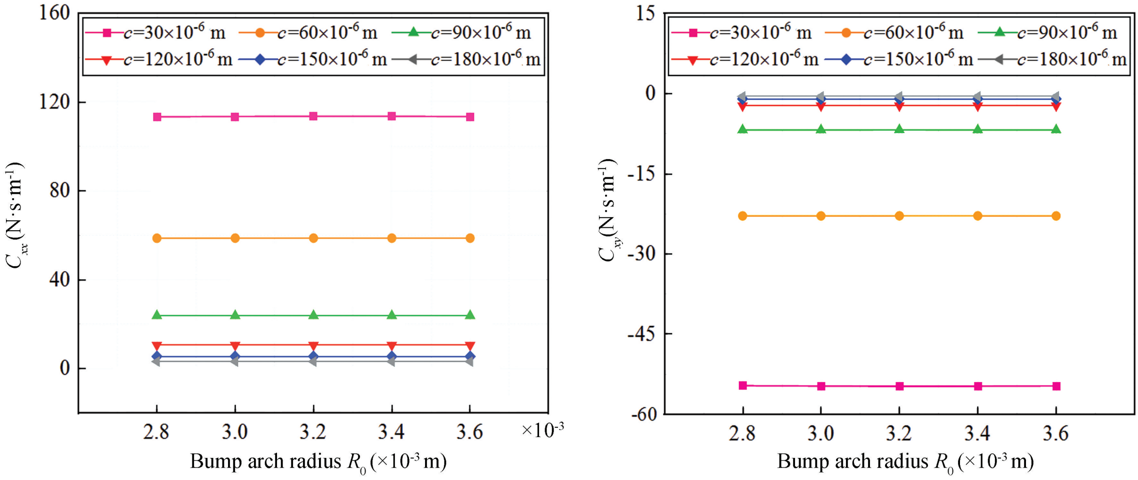

(a) C_{xx} (b) C_{xy}

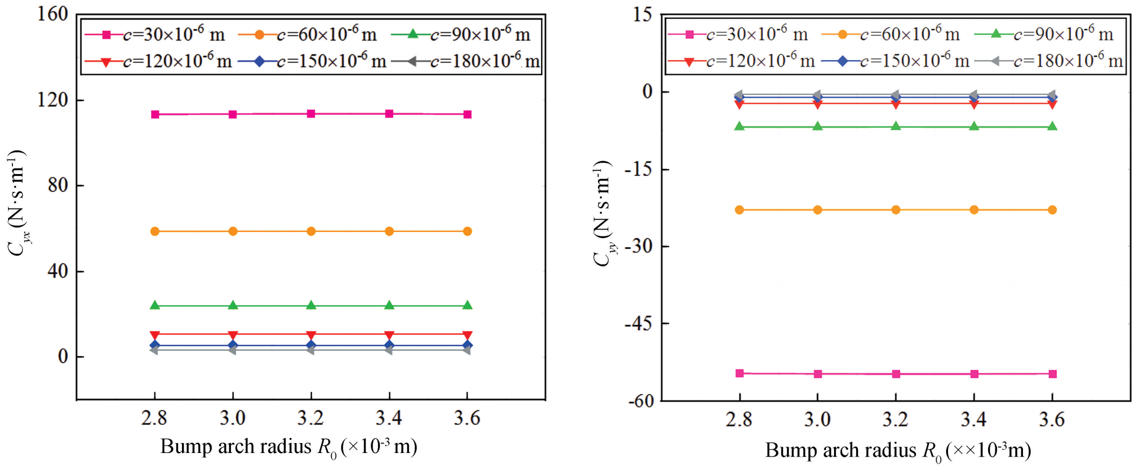

(c) C_{yx}

(d) C_{yy}

Fig.25 Damping coefficients versus bump arch radius

3 Conclusions

1) A mechanical model simplifying the foil structure of the bearing as a two-dimensional thin plate finite element model with an elastic support is established by use of the theory of elasticity. The calculation model comprehensively considers the frictions and the interactive forces of bumps. A fluid-solid coupling model for the bearing is established using the compressible gas Reynolds equation. The perturbation method is applied to develop a dynamic model. Using the finite difference method and MATLAB programming, a precise calculation method for lubrication and dynamic performances is established. The friction torque measurements experimentally validated the reliability of the theoretical model.

2) The lubrication performances under varying radial clearances and rotational speeds are investigated. $P_{\max}$ increases and $H_{\min}$ decreases with radial clearance. $P_{\max}$ decreases and $H_{\min}$ increases with rotational speed. The maximum load capacity decreases with radial clearance and increases with rotational speed. Friction torque and friction power loss decrease with radial clearance and increase with rotational speed. The side leakage flow rate of gas increases with radial clearance and rotational speed.

3) The lubrication performances under varying foil structural parameters are investigated. The maximum load capacity, friction torque, and friction power increase with top and bump foil thickness but decrease with bump arch half-length. Besides, the maximum load capacity, friction torque, friction power loss and side leakage flow rate of gas are almost unaffected by bump arch radius.

4) The dynamic performances under varying radial clearances and rotational speeds are investigated. The main stiffness coefficients decrease with radial clearance and increase with rotational speed, which echoes the situation where the maximum load capacity varies with radial clearance. The main damping coefficients decrease with radial clearance and rotational speed.

5) The dynamic performances under varying foil structural parameters are investigated. The main stiffness coefficients increase with top and bump foil thickness and bump arch half-length. The main damping coefficients increase with top and bump foil thickness, but decrease with bump arch half-length. It is noted that the influences become more significant with smaller radial clearances. In addition, the eight dynamic coefficients are almost unaffected by the bump arch radius. The above research results will provide guidance for the design and manufacturing of air foil journal bearings.

Nomenclature

Λ	Bearing number
c	Bearing radial clearance
e	Bearing eccentricity
ε	Bearing eccentricity ratio
H_0, P_0	Dimensionless air film thickness and pressure during static equilibrium
I_t	Sectional moment of inertia
λ	Dimensionless bearing axial width
ρ	Gas density
θ	Bearing circumferential coordinate
R	Shaft radius
$\mathscr{R}$	Gas constant
T	Thermodynamic temperature
τ_e	Dimensionless time
U	Shaft linear velocity
v	Whirl frequency ratio
$\overline{\Delta x}$	$\Delta x/c$, horizontal dimensionless perturbation displacement
$\overline{\Delta x'}$	$\Delta x'/c$, horizontal dimensionless perturbation velocity
$\overline{\Delta y}$	$\Delta y/c$, vertical dimensionless perturbation displacement
$\overline{\Delta y'}$	$\Delta y'/c$, vertical dimensionless perturbation velocity

References

[1] Guo Z, Feng K, Liu T, et al. Nonlinear dynamic analysis of rigid rotor supported by gas foil bearings: Effects of gas film and foil structure on subsynchronous vibrations. Mechanical Systems and Signal Processing, 2018, 107: 549-566. DOI: 10.1016/j.ymssp.2018.02.005.

[2] DellaCorte C. Oil-free shaft support system rotordynamics: Past, present and future challenges and opportunities. Mechanical Systems and Signal Processing, 2012, 29: 67-76. DOI: 10.1016/J.YMSSP.2011.07.024.

[3] Branagan M, Griffin D, Goyne C, et al. Compliant gas foil bearings and analysis tools. Journal of Engineering for Gas Turbines and Power, 2016, 138(5): 054001. DOI: 10.1115/1.4031628.

[4] Walowit J A, Anno J N, Hamrock B J. Modern Developments in Lubrication Mechanics. London: Applied Science Publishers Ltd, 1975: 214-221.

[5] Heshmat H, Shapiro W, Gray S. Development of foil journal bearings for high load capacity and high speed whirl stability. Journal of Lubrication Technology, 1982, 104(2): 149-156. DOI: 10.1115/1.3253173.

[6] Heshmat H. Operation of foil bearings beyond the bending critical mode. Journal of Tribology, 2000, 122(1): 192-198. DOI: 10.1115/1.555342.

[7] Radil K, Howard S, Dykas B. The role of radial clearance on the performance of foil air bearings. Tribology Transactions, 2002, 45(4): 485-490. DOI: 10.1080/10402000208982578.

[8] Lee D H, Kim Y C, Kim K W. The static performance analysis of foil journal bearings considering three-dimensional shape of the foil structure. Journal of Tribology, 2008, 130(3): 031102. DOI: 10.1115/1.2913538.

[9] DellaCorte C, Radil K C, Bruckner R J, et al. Design, fabrication, and performance of open source generation I and II compliant hydrodynamic gas foil bearings. Tribology Transactions, 2008, 51(3): 254-264. DOI: 10.1080/10402000701772579.

[10] Schiffmann J, Spakovszky Z S. Foil bearing design guidelines for improved stability. Journal of Tribology, 2013, 135(1): 011103. DOI: 10.1115/1.4007759.

[11] Xu H, Yang J, Gao L, et al. The influences of bump foil structure parameters on the static and dynamic characteristics of bump-type gas foil bearings. Proceedings of the Institution of Mechanical Engineers, Part J: Journal of Engineering Tribology, 2020, 234(10): 1642-1657. DOI: 10.1177/1350650120912609.

[12] Luan W, Liu Y, Wang Y, et al. Effect of herringbone groove structure parameters on the static performance of gas foil herringbone groove thrust bearings. Tribology International, 2023, 177: 107979. DOI: 10.1016/j.triboint.2022.107979.

[13] Mahner M, Li P, Lehn A, et al. Numerical and experimental investigations on preload effects in air foil journal bearings. Journal of Engineering for Gas Turbines and Power, 2018, 140(3): 032505. DOI: 10.1115/1.4037965.

[14] Mahner M, Bauer M, Lehn A, et al. An experimental

investigation on the influence of an assembly preload on the hysteresis, the drag torque, the lift-off speed and the thermal behavior of three-pad air foil journal bearings. Tribology International, 2019, 137: 113 – 126. DOI: 10.1016/J.TRIBOINT.2019.02.026.

[15] Mahner M, Bauer M, Schweizer B. Numerical analyzes and experimental investigations on the fully-coupled thermo-elasto-gasdynamic behavior of air foil journal bearings. Mechanical Systems and Signal Processing, 2021, 149: 107221. DOI: 10. 1016/J. YMSSP. 2020. 107221.

[16] Kim D. Parametric studies on static and dynamic performance of air foil bearings with different top foil geometries and bump stiffness distributions. Journal of Tribology, 2007, 129(2): 354 – 364. DOI: 10. 1115/1. 2540065.

[17] Shi T, Huang H, Peng X, et al. Experimental study on the static and dynamic performances of gas foil bearings for the centrifugal air compressor used in fuel cell vehicles. International Journal of Energy Research, 2022, 46(4): 4417–4433. DOI: 10.1002/er.7439.

[18] Shi T, Chen Z, Zhang J, et al. Performances investigation and multi-objective optimization of gas foil bearings in hydrogen fuel cell vehicles. International Journal of Energy Research, 2022, 46(13): 18849–18865. DOI: 10.1002/er. 8507.

[19] Shi T, Huang H, Chen Q, et al. Performance investigation and feasibility study of novel gas foil thrust bearing for hydrogen fuel cell vehicles. International Journal of Energy Research, 2022, 46(9): 12642 – 12659. DOI: 10.1002/er.8033.

[20] Guan H, Feng K. Static and dynamic characteristics of gas foil bearing with piezoelectric-Metal Mesh Blocks. Chinese Journal: Bearing, 2022(10): 76–85. DOI: 10.19533/j. issn1000–3762.2022.10.011.

[21] Sim K, Lee Y B, Kim T H. Effects of mechanical preload and bearing clearance on rotordynamic performance of lobed gas foil bearings for oil-free turbochargers. Tribology Transactions, 2013, 56(2): 224 – 235. DOI: 10.1080/10402004.2012.737502.

[22] Walter F, Sinapius M. Influence of aerodynamic preloads and clearance on the dynamic performance and stability characteristic of the bump-type foil air bearing. Machines, 2021, 9(8): 178. DOI: 10.3390/machines9080178.

[23] Xiong C, Xu B, Yu H, et al. Static and dynamic characteristics of aerodynamic thrust bearings based on fluid-thermal-structural interaction approach. Thermal Science and Engineering Progress, 2023, 42: 101901. DOI: 10.1016/j.tsep.2023.101901

[24] Cheng W, Zhu Y, Ke H, et al. Identification of dynamic coefficients of gas foil bearings by simulated excitation based on coupled fields. Advances in Mechanical Engineering, 2024, 16(5): 16878132241253402. DOI: 10. 1177/16878132241253402

[25] Zhao Q, Qiang M, Yan S, et al. Frictional analysis on stiffness and damping characteristics of bump foil gas bearings. Proceedings of the Institution of Mechanical Engineers, Part J: Journal of Engineering Tribology, 2023, 237 (3): 498 – 513. DOI: 10. 1177/ 13506501221132110.

[26] Arghir M, Benchekroun O. A simplified structural model of bump-type foil bearings based on contact mechanics including gaps and friction. Tribology International, 2019, 134: 129–134. DOI: 10.1016/J.TRIBOINT.2019.01.038.

[27] Gu Y, Ren G, Zhou M. A fully coupled elastohydrodynamic model for static performance analysis of gas foil bearings. Tribology International, 2020, 147: 106297. DOI: 10.1016/j.triboint.2020.106297.

[28] Xu Z, Li C, Du J. Modeling and static characteristics study of the double–layer bump gas foil bearing. Tribology International, 2021, 164: 107202. DOI: 10. 1016/J. TRIBOINT.2021.107202.

[29] Xu F, Dong Z, Chu J, et al. Experimental analysis of influence of double – layer bump foils on aerodynamic thrust foil bearings performance. Industrial Lubrication and Tribology, 2022, 74(1): 127–133. DOI: 10.1108/ILT–07–2021–0281.

[30] Li C, Du J, Li J, et al. Investigations on the load capacity of multilayer foil thrust bearing based on an updated complete model. Journal of Tribology, 2023, 145(2): 021202. DOI: 10.1115/1.4055130.

[31] Liang B, Luo X, Ning J, et al. Study on bearing performance of gas foil bearing based on three-dimensional finite element bump foil model. Chinese Journal: Energy Conservation Technology, 2021, 39(4): 332–338. DOI: 10.3969/j.issn.1002–6339.2021.04.008.

[32] Gu Y, Ren G, Zhou M. A novel method for calculating the dynamic force coefficients of Gas Foil Bearings and its application in the rotordynamic analysis. Journal of Sound and Vibration, 2021, 515: 116466. DOI: 10.1016/j.jsv. 2021.116466.

[33] Zhou R. Hysteresis behaviors of a bump-type foil bearing structure with amended lugre friction model. Proceedings of the 23rd Pacific Basin Nuclear Conference. Singapore: Springer Nature Singapore, 2023: 342 – 354. DOI: 10. 1007/978–981–99–1023–6_31

[34] Qi S, Ho Y, Geng H, et al. A theoretical study on the influence of frequency on the dynamic characteristics of air film. Key Engineering Materials, 2011, 462–463: 817–824. DOI: 10. 4028/www. scientific. net/KEM. 462 – 463. 817.

[35] Ruscitto D, McCormick J, Gray S. Hydrodynamic Air Lubricated Compliant Surface Bearing For An Automotive Gas Turbine Engine I– Journal Bearing Performance. New York: Office of Scientific and Technical Information, 1978.